Meteorol. Atmos. Phys. 74, 129–157 (2000)

Meteorology and Atmospheric Physics

Department of Marine, Earth and Atmospheric Sciences, North Carolina State University, Raleigh, NC

Mesoscale simulations of dynamical factors discriminating between a tornado outbreak and non-event over the southeast US Part I: 84–48 hour precursors

J. M. Egentowich, M. L. Kaplan, Y.-L. Lin, and **A. J. Riordan**

With 28 Figures

Received December 23, 1999
Revised January 16, 2000

Summary

Observational analysis and mesoscale numerical simulations are in agreement concerning key dynamical processes which occurred over Mexico and the Gulf of Mexico 84 hours prior to the 1988 Raleigh (RDU), NC tornado outbreak. The subtropical jet (STJ) over northern Mexico and its associated transverse ageostrophic circulation forced air down the eastern side of the Sierra Madre Mountains creating adiabatic warming due to compressional heating. Along with this warm air, a low-level trough of low pressure formed and a low-level jet (LLJ) developed over the western Gulf of Mexico. This LLJ began the process that transported very warm and potential vorticity (*PV*) rich air from the Mexican plateau to the Carolina Piedmont.

The low-level *PV* maximum over central NC at the time of the tornado was a coherent entity traceable back 84 hours to the Mexican plateau. Over the Mexican plateau, the STJ transported the *PV* rich air southward then down to the midlevels. There was substantial heating over the plateau producing a deep well-mixed layer and a mountain-plains solenoid. An area of strong vertical convergence developed in the 500–600 hPa layer which increased the thermal gradient and maintained the *PV*. This mid-level *PV* was transported to the low-levels by a hydrostatic mountain wave. As the *PV* maxima moved down the lee of the mountains it increased due to strong static stability, tilting and frictional effects. Finally, the *PV* maxima moved along the Gulf Coast and up the East Coast to central NC.

1. Introduction

The Raleigh, NC tornado of 28 November 1988 was an extraordinary event, which has stimulated a great deal of interest from the weather forecasting and research communities. This tornado occurred in the middle of the night in late November with an unusual F4 (for NC) intensity. This devastating tornado was on the ground for 83 miles resulting in 4 deaths, 154 injuries, and an estimated 77.2 million dollars in property damage (NOAA 1988). It occurred in the vicinity of the polar jet (PJ) entrance region, not the exit region, where previous jet dynamical paradigms have focused (e.g. Kaplan and Paine, 1977; Uccellini and Johnson, 1979; Kocin et al., 1985, 1986; Zack and Kaplan, 1987). The severe weather at Raleigh was part of a larger outbreak near the PJ entrance region, which produced numerous tornadoes over NC and VA. The National Weather Service didn't issuing any severe weather watch or warning prior to observations of severe weather, in part, because the severe weather predictive indices based upon typical jet exit region dynamics were unremarkable (Gonski et al., 1989). Also, the severe weather occurred within a region of negative 500 mb vorticity advection and weak low-level warm advection thus minimizing typical quasi-geostrophic (QG) indicators of severe weather potential (Gonski, 1989). The inability of standard indices/dynamical paradigms to indicate at least modest tornadic potential for such an

extreme event is reasonable because most of our severe weather prediction paradigms were implicitly based on the PJ streak exit region model. The ambiguity of the Raleigh tornado case study indicates that more research is needed to understand the mechanisms that produce severe weather in the southeast US.

Upper level jet streaks and their associated transverse ageostrophic circulations are often the driving force for surface weather. The transverse circulations about the jet streak develop so the atmosphere maintains a balance between the mass and momentum fields in an effort to maintain a QG state. The upper-level jet streak and its associated transverse ageostrophic circulation are coupled to the low-level circulation (Uccellini and Johnson, 1979).

A potential complicating issue to the Uccellini and Johnson paradigm (1979) proposed by Uccellini and Kocin (1987) and applied in Kaplan et al. (1998) is the juxtapositioning of the PJ streak and subtropical jet (STJ) streak (Fig. 1). The two transverse ageostrophic circulations, associated with the jet streaks, phase in a manner which produces an area of intense and deep vertical motion; the direct circulation, associated with the PJ entrance region, phases with the indirect circulation accompanying the STJ exit region. Between the two upper-level jet streaks there is confluence in the low levels, ascent through the column, and difluence in the upper levels. With both jet streaks producing divergence aloft over the same area one would intuitively expect a substantial amount of mass removed from the column of air.

Kaplan et al. (1998) proposed a new paradigm, with three primary concepts, for severe weather development over the southeast US. First, the juxtapositioning of the PJ entrance region and the STJ exit region and their transverse secondary circulations create deep QG vertical motions. Second, geostrophic adjustment of the mass field to the wind field occurs near the continental air and polar air interface, i.e., low-level fronts accompany the return branch of the STJ streak and return branch of the PJ streak resulting in an unbalanced mid-tropospheric mesoscale jet streak or jetlet. Third, a parcel undergoes stretching and tilting as it is caught up in the thermally direct unbalanced circulation in the right front quadrant of the geostrophically adjusting jetlet.

The secondary circulations associated with the PJ and STJ transport air from very different source regions, producing a strong cross-stream frontal zone, and an unbalanced, mid-level jetlet. The jetlet is unbalanced because it is constantly accelerating under the STJ exit region where it normally would be decelerating. The exit region of the developing jetlet is a region of extreme thermal wind imbalance since vertical motions are no longer balanced, i.e., accelerations occur where the Uccellini and Johnson (1979) paradigm proposes decelerating flow. The unbalanced jetlet, and ascent, extends over the tropical air creating a longer and more intense destabiliza-

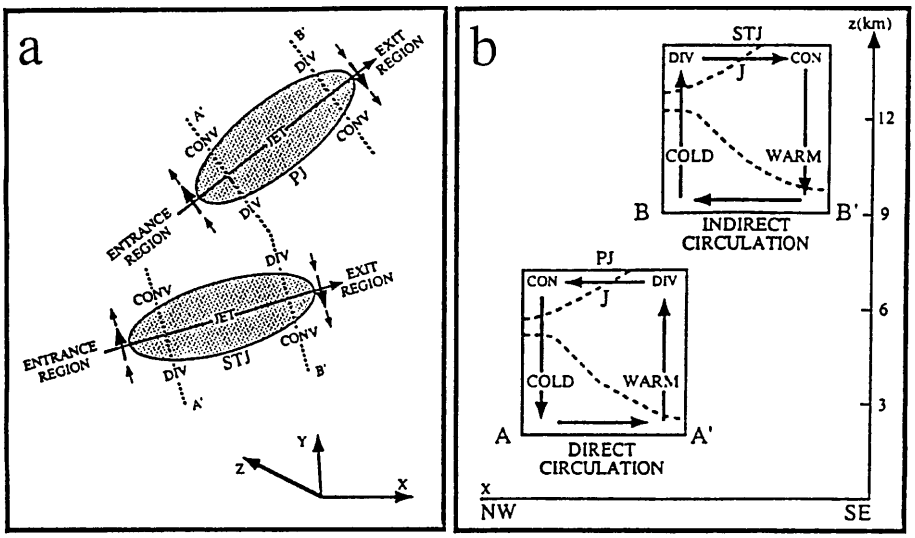

Fig. 1. Schematics depicting **a** horizontal and **b** vertical structures of the transverse ageostrophic cicrulations about the polar and subtropical jet streaks from Kaplan et al. (1998)

tion and the formation of severe weather to the right of the QG-balanced PJ. That is because air parcels converging into the unbalanced region can be more rapidly destabilized as they have larger convective available potential energy (CAPE).

It is assumed that a favorable large-scale hydrostatic environment, which is rich in rotational energy (cyclonic vorticity), is necessary for convective storms to produce focused vortices such as tornadoes. There are four ways in which the environment can contribute rotational energy to intensifying convection: (1) through the convergence of vorticity, (2) vertical wind shears that enhance the tilting of horizontal vorticity into the vertical, (3) baroclinically-generated vorticity (solenoidal maxima), and (4) frictionally generated vorticity. A hydrostatic environment rich in potential vorticity (*PV*), i.e., the product of the vertical vorticity and static stability, is likely to be an environment which favors the intensification of supercell convection into rotating convection because of all four of these forcing mechanisms.

First, by definition, a significant magnitude of environmental *PV* cannot be separated from the magnitude of the vertical component of vorticity. Second, strong horizontal wind shears accompanying vertical vorticity maxima imply vertical shears as they often occur near thermal boundaries or highly confluent circulations. Therefore, high vorticity often implies high vertical shear. Third, thermal boundaries, fronts, and highly confluent circulations are typically baroclinic/solenoidal in structure. Strong vertical potential temperature gradients are typically associated with large horizontal gradients of potential temperature near fronts and, hence near solenoids. Fourth, friction may generate new *PV*. Therefore, *PV* is an excellent tracer for the potential rotational energy if it can be combined with a favorable environment for the generation and maintenance of convection.

Gyakum et al. (1995) related the diabatic production of *PV* to rapid surface cyclogenesis. Gyakum found horizontal gradients of grid-scale latent heating produced a mid-tropospheric *PV* anomaly that was related to rapid surface frontogenesis. Also, surface sensible heating created a boundary layer anomaly, which interacted with the mid- and upper-level *PV* maxima resulting in rapid surface cyclogenesis. Finally, this study concluded that surface frontogenesis produced a vertical wind shear enhancing the diabatic generation of *PV* through tilting. Zehnder and Keyser (1991) investigated rapid cyclogenesis in the absence of diabatic effects. They found the interaction between upper- and lower-level disturbances characterized by nonuniform *PV* results in a significant increase in relative vorticity at the surface.

Potential vorticity in the midlevels (in isobaric coordinates) may be estimated by:

$$PV = \underbrace{-\frac{\partial\theta}{\partial p}(\zeta_p + f)}_{1} \underbrace{-\hat{k}\cdot\frac{\partial\vec{V}_h}{\partial p}\times\nabla_p\theta}_{2}. \qquad (1)$$

Term 1 represents the contribution due to absolute vorticity on a pressure surface in a statically stable environment. Term 2 represents the contribution due to the tilting of isentropic surfaces and is expected to be important in an area of an intense baroclinic zone. *PV* is often estimated using only term 1; however, in this study term 2 is essential to understanding the underlying physical processes that separate a severe weather event from a non-severe event. Term 1 is typically associated with a balanced QG fold as in a nonsevere weather event while term 2 is associated with unbalanced tilting and is more important in a severe weather event. The generation of mesoscale *PV* may be examined in isentropic coordinates using the Lagrangian *PV* equation (Gidel and Shapiro, 1979):

$$\frac{d}{dt}\left[-(\zeta_\theta + f)\frac{\partial\theta}{\partial p}\right] = \underbrace{-(\zeta_\theta + f)\frac{\partial}{\partial p}\left(\frac{d\theta}{dt}\right)}_{1} \underbrace{-\left(\frac{\partial\theta}{\partial p}\right)\hat{k}\cdot\nabla_\theta\times\vec{F}}_{2} + \underbrace{\left(\frac{\partial\theta}{\partial p}\right)\hat{k}\cdot\nabla_\theta\left(\frac{d\theta}{dt}\right)\times\frac{\partial\vec{V}}{\partial\theta}}_{3}. \qquad (2)$$

Term one relates to the production or destruction of *PV* due to vertical gradients of diabatic heating with isentropic absolute vorticity. This term is often called the stability change term since it is related to the changes in static stability

$\frac{\partial\theta}{\partial p}$ due to heating (or cooling) across a layer. Term two represents the change in *PV* resulting from frictional stresses (*F*). Term three represents the change in *PV* resulting from the tilting of the horizontal component of vorticity into the vertical through horizontal diabatic heating. In the low-levels, terms 2 and 3 are the main mechanism for *PV* production and maintenance.

In this paper, we will explore the relationship between the existence of the STJ and its effects on the lower environment (associated mass and momentum adjustments, development of a LLJ, and low-level *PV*) 84–48 hours before the development of severe weather (tornado event over central NC on 28 November 1988). Also, we will compare the environment of the RDU tornado event to a synoptically similar event where severe weather was forecast but none developed over central NC (25 January 1990). In the two companion papers our investigation of the pre-tornadic environment will contract in both temporal and spatial resolution. Section 2 will compare the synoptic situations of the event and non-event cases. Section 3 will describe the mesoscale model used to simulate the early environment. Section 4 deals with the origins of airmasses at different levels over central NC at the time of the event and non-event. Section 5 examines the numerical simulations of these two cases. In Section 6 we will investigate the origins of low-level PV. Finally, in Section 7 we will summarize and present our conclusions.

2. Event and non-event comparison

In this series of papers, we compare the mesoscale environment of a tornadic weather event of 28 November 1988 at 0600 UTC (referred to as event) to that of a non-event of 25 January 1990 (referred to as non-event). In the later case, the Raleigh NWS office (Gonski, personal communication, 1998) expected severe weather to develop over central NC at 1800 UTC (designated as the onset of the non-event). The convective outlook and second day severe outlook were forecasting severe thunderstorms across the Piedmont, with possible isolated tornadoes over GA. AT 1437 UTC, the National Severe Storms Forecast Center (Kansas City) issued a severe thunderstorm watch for central GA, SC and NC valid from 1400 to 2000 UTC. The window of the non-event ends when the front moves over the Piedmont near 0000 UTC 26 January 1990. Since the actual time of the non-event is ambiguous we will examine the non-event over a period of time starting at 1800 UTC 25 and ending 0000 UTC 26 January 1990. Since the synoptic situations were so similar and yet there were dramatic differences in the outcome, there must be some crucial and subtle difference(s) that greatly enhanced the potential for severe weather. A direct comparison between these cases should highlight these differences. In the event case, no severe weather was forecasted in NC yet an F4 tornado originated near RDU and traveled northeast. In the non-event case, severe weather was expected by the local NWS office and from the National Severe Storm Prediction Center but did not materialize over NC.

We perform an in-depth comparison between the event and the expected onset time of the non-evnt cases. Comparisons back 6, 24 and 48 hours are synoptically similar in many ways but 72 hours prior to event there are striking synoptic differences. For the sake of brevity we will highlight the comprison using the NWS analysis six hours before each event: 0000 UTC, 28 November 1988 to 1200 UTC, 25 January 1990.

In both cases, the 200 hPa analysis (Fig. 2a, b) depict a deep trough of low pressure extending north-south from MN to western TX. The orientation of the troughs is the same for the two cases. The PJ extends from eastern TX over the Appalachian Mountains and northeast to Quebec. Over the southeastern states, the directions of observed winds are displaced to the right of the height contours indicating supergeostrophic speeds. Also, the winds are stronger over the southeastern states (due to the STJ) in the event case. The temperature pattern is very similar between the two cases. The event case STJ and PJ are clearly depicted in Fig. 2c, a cross section based on observations.

The 500 hPa analysis (Fig. 3a, b) depicts a deep trough of low heights over the central part of the continent with a pronounced low over MI and WI. The orientation of the trough of low heights extends back over the Big Bend region of TX. The jet extends from northeast TX over WV and into Canada. In both cases, the wind speed and

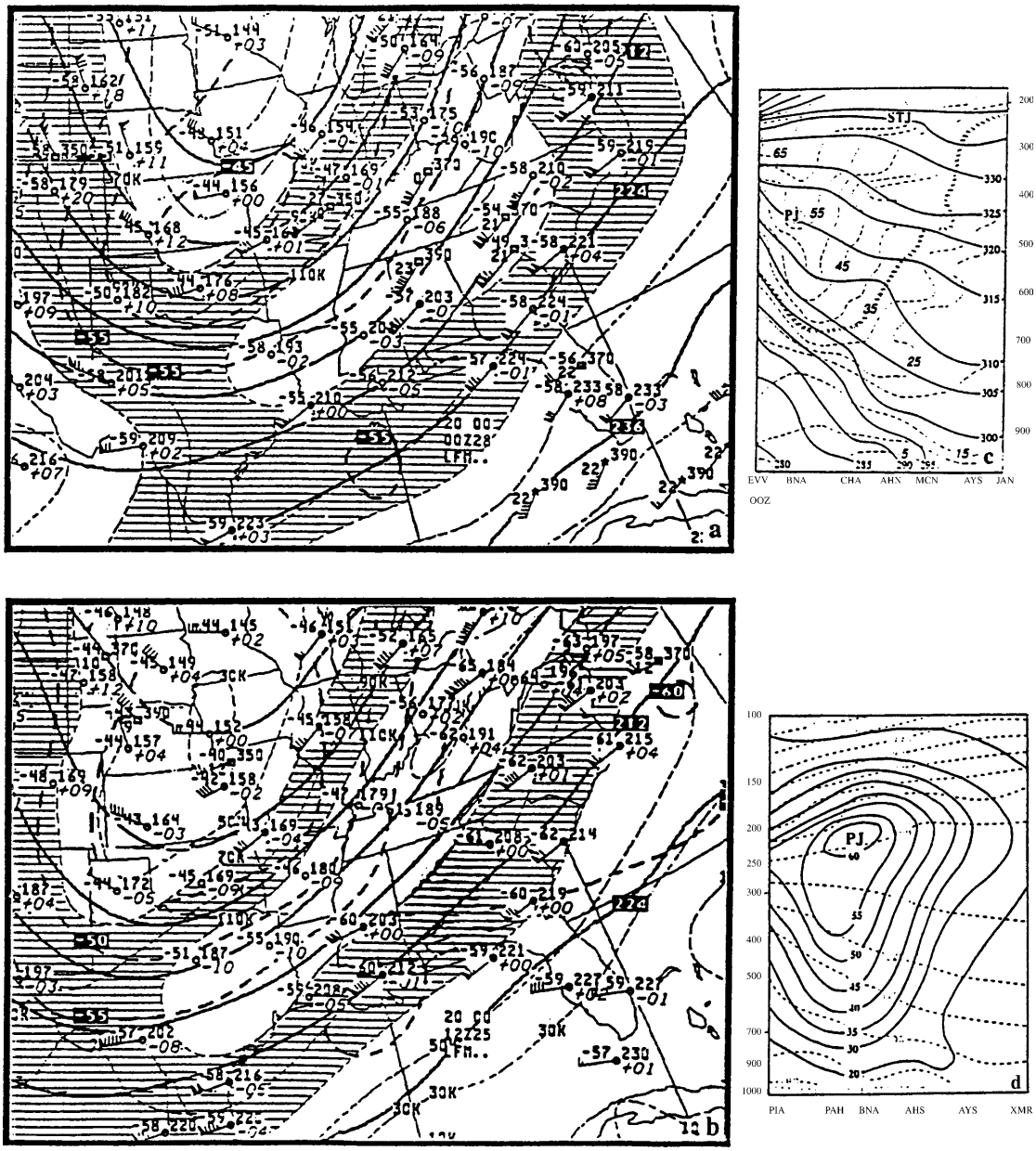

Fig. 2. a NWS 200 hPa analysis of isotachs (knots) and vectors, temperature (C) and height (dm) and **c** observation derived cross section from Evansville, IN (EVV) to Jacksonville, FL (JAX), isotachs (dashed line, ms^{-1}) and θ (solid line, K) valid at 0000 UTC 28 November 1988; **b** NWS 200 hPa analysis of isotachs and vectors (knots), temperature (C) and height (dm) and **d** observationally derived cross section from Peoria, IL (PIA) to Cape Kennedy, FL (XMR) isotachs (solid line, ms^{-1}) and θ (dashed line, K) valid at 1200 UTC 25 January 1990

direction, over the southeastern states are similar. The height gradient is slightly weaker over MI to OH in the 1990 case translating to a slightly weaker mid-level jet over the Piedmont. Also, the temperature pattern is very similar in both cases.

The 850 hPa analysis (Fig. 4a, b) depicts a low over the northern Midwest with a trough extending over the TN valley and to central LA. In the 1988 case, a low is beginning to cut off over northern WI with a minimum height of 128 dm. In the 1990 case, the low has cut

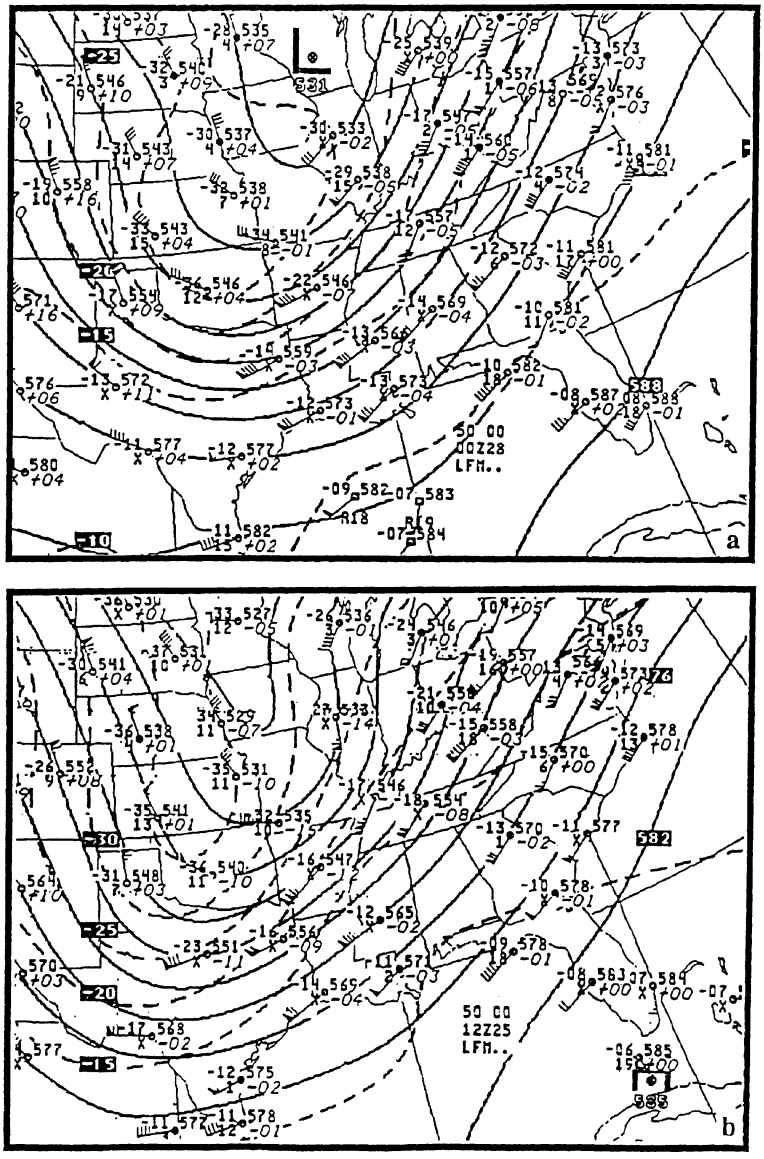

Fig. 3. NWS 500 hPa analysis of wind vectors, temperture (C), and height (dm) valid at **a** 0000 UTC 28 November 1988, and **b** 1200 UTC 25 January 1990

off over northern IL with a minimum height of 128 dm. The band of maximum wind is orientated from southwest to northeast over the southeastern US. The temperature field is similar in both the cases except that temperatures were 2–4 °C warmer in the 1988 case over the southeast US.

The 0035 UTC 28 November 1988 and 1235 UTC 25 January 1990 radar summaries (Fig. 5a, b) have many similarities. There is a line of rain and thunderstorms along the Carolina coast and a precipitation free region over the Piedmont. A line of heavy thunderstorms is over the SC and GA border, moving into central NC at 26 to 31 ms^{-1}. However, the height of convection is significantly higher in the 1988 case, 14 km versus 8.1 km. In addition, the event case has more clusters of enhanced reflectivity indicating more convective instability.

3. Model summary

Due to the lack of high-resolution observational data, numerical simulations must be employed to understand the environments prior to the event and non-event. The MASS model used in this study is a modified version of the model originally developed by Kaplan et al. (1982).

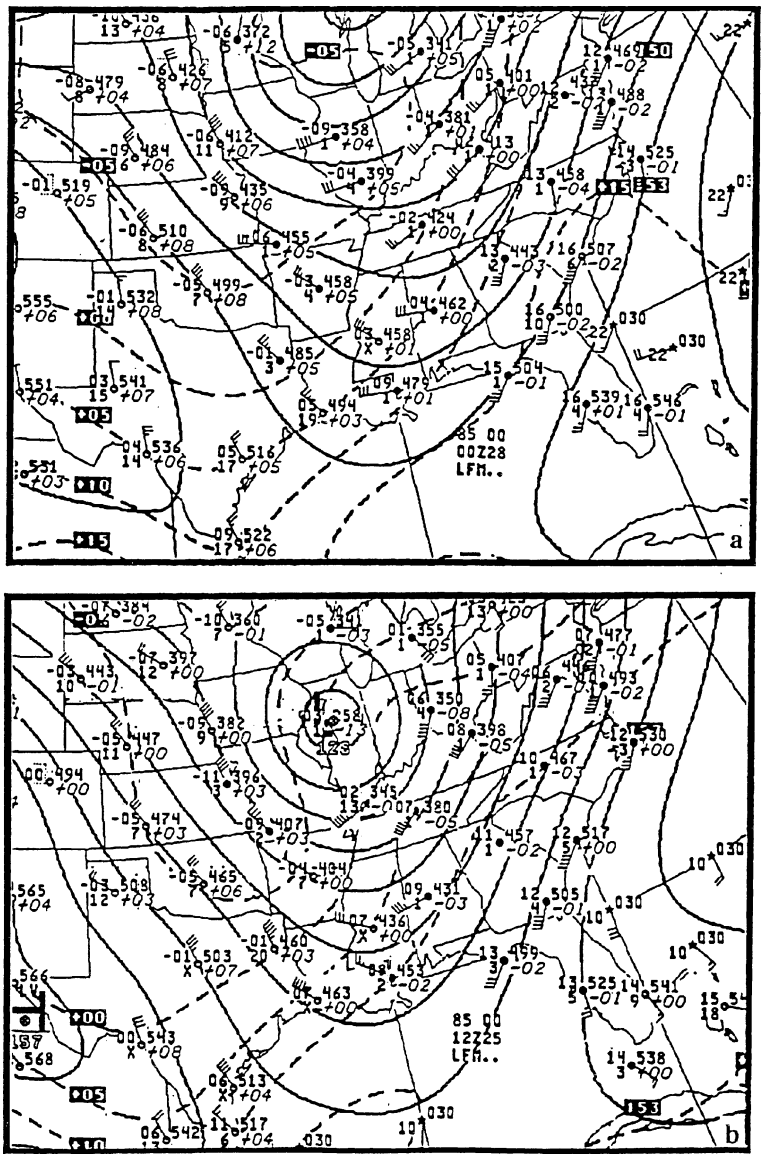

Fig. 4. NWS 850 hPa analysis of wind vectors, temperature (C), and height (dm) valid at **a** 0000 UTC 28 November 1988, and **b** 1200 UTC 25 January 1990

The numerical experiments used in this series of papers are summarized in Table 1. The grid resolution and coverage are shown in Figs. 6a and b. The model specifics are summarized in the following (MESO 1995):

Model numerics:

1. Hydrostatic primitive equation model (3-D equations for u, v, T, q & p),
2. Vertical resolution is 37 sigma layers for the 72 km run and 40 layers for the 24 & 12 km run,
3. Energy absorbing upper sponge layer,
4. Terrain following sigma-p coordinate system,
5. A 30 second short timestep for the gravity wave mode (forward-backward scheme),
6. A 90 second long timestep for the slow advection mode (split-explicit time marching integration using the Adams-Bashforth scheme).

Initialization scheme:

1. A first guess using NMC/NCAR reanalyzed gridded data (2.5×2.5 lat/long grid & 17 levels),
2. Reanalysis using 3-D OI scheme (Daley 1991),
3. High resolution average terrain using one pass 9 point smoother,

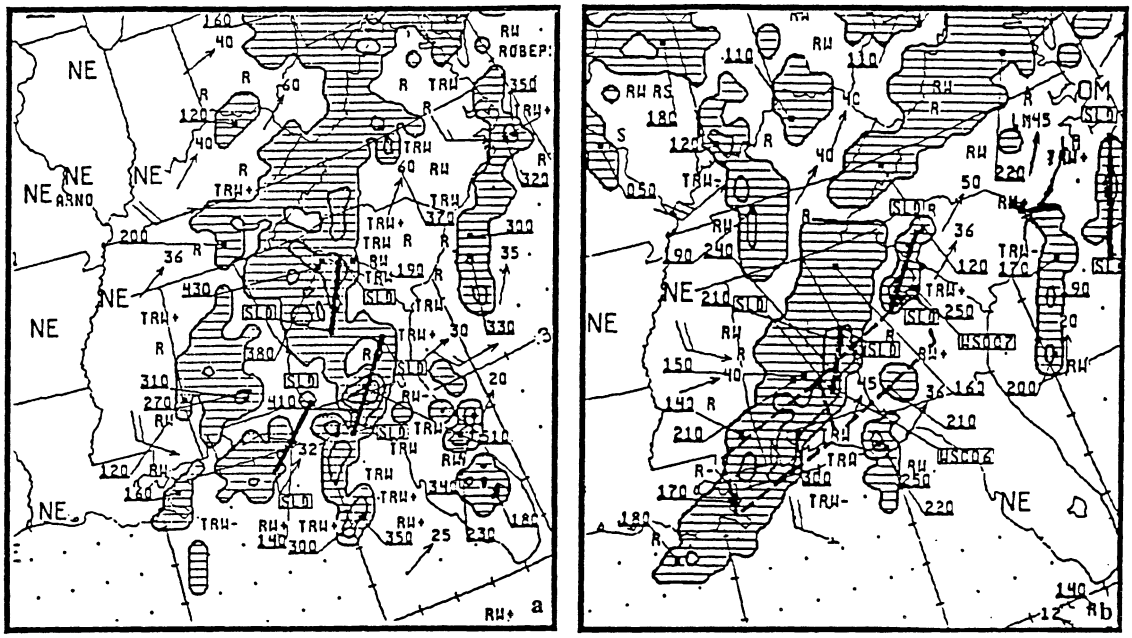

Fig. 5. NWS radar summaries valid at **a** 0035 UTC 28 November 1988, and **b** 1235 UTC 25 January 1990

Table 1. The MASS modeling simulations performed in the study

Initialization (UTC)	Duration (hours)	Resolution (km)	Matrix size (x, y, z)	Modifications
1200 UTC 24 Nov 88	24	24	170, 130, 40	None
0000 UTC 25 Nov 88	72	72	130, 110, 37	None
0000 UTC 22 Jan 90	24	24	170, 130, 40	None
1200 UTC 22 Jan 90	72	72	130, 110, 37	None
0000 UTC 25 Nov 88	36	24	170, 130, 40	None
1200 UTC 23 Jan 90	36	24	170, 130, 40	No latent heating
1200 UTC 23 Jan 90	36	24	170, 130, 40	None
0000 UTC 26 Nov 88	36	24	170, 130, 40	No latent heating
0000 UTC 26 Nov 88	36	24	170, 130, 40	None
1200 UTC 24 Jan 90	36	24	170, 130, 40	No latent heating
1200 UTC 24 Jan 90	36	24	170, 130, 40	None
0000 UTC 27 Nov 88	36	24	205, 155, 40	No latent heating
0000 UTC 27 Nov 88	36	24	205, 155, 40	None
1200 UTC 27 Nov 88	24	24	205, 155, 40	Yes, MDR data
1200 UTC 27 Nov 88	24	12	205, 155, 40	None
1200 UTC 24 Jan 90	36	24	205, 155, 40	None
1200 UTC 24 Jan 90	36	24	205, 155, 40	No latent heating
0000 UTC 25 Jan 90	24	24	205, 155, 40	Yes, MDR data
0000 UTC 25 Jan 90	24	12	205, 155, 40	None

4. Ehanced moisture analysis through synthetic RH retrieval scheme,
5. Weekly averaged 1×1 latitude/longitude sea surface temperature data,
6. Anderson level II land use classification scheme,
7. Climatological subsoil moisture database,
8. Normalized difference vegetation index (NVDI).

Planetary boundary layer physics:

1. A modified Blackadar high resolution PBL scheme (Zang and Anthes 1982),

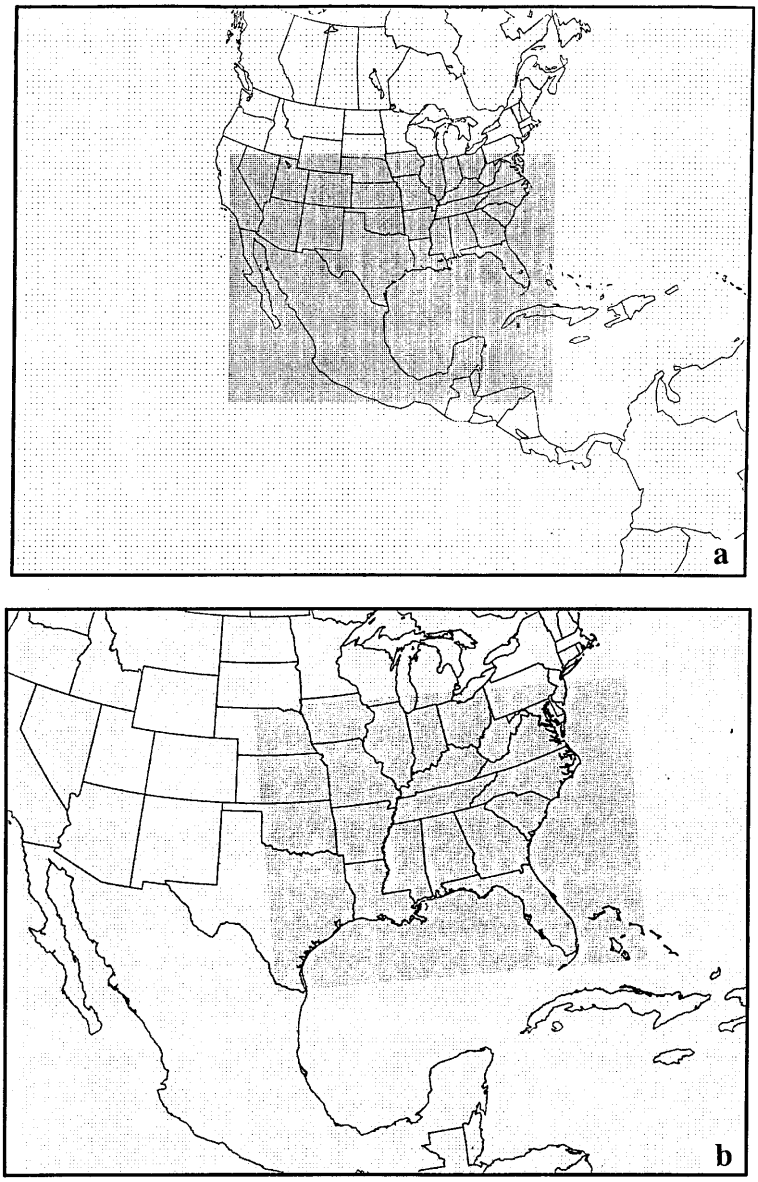

Fig. 6. Area of integration for simulations used in this study; **a** depicts area of 72 km (130×110) and 24 km (170×130) simulations, and **b** depicts area of 24 km (205×155) and 12 km (205×155) simulations

2. A surface energy budget based on the Noilhan and Planton scheme (1989),
3. Soil hydrology based on the Mahrt and Pan scheme (1984).

Moisture physics:

1. Grid scale bulk parameterization of cloud water & ice, rainwater and snow (Zang 1989, Lin et al. 1983),
2. Sub-grid scale Kuo-MESO convective parameterization scheme.

The NMC/NCAR reanalysis project (Kalnay et al., 1996) provided the first guess fields for producing the database which is used to initialize the numerical model. The dataset is reanalyzed using radiosonde ballon data and aviation surface data sets from the hourly observational network using a 3D-Optimal Interpolation (3DOI) scheme (Daley, 1991). The grid resolutions are 72 km, 24 km, or 12 km, centered at 60° N. Simulations are centered over 36° N so the actual resolution, taking map distortion into account, is much finer (57 km, 19 km, or 9.5 km).

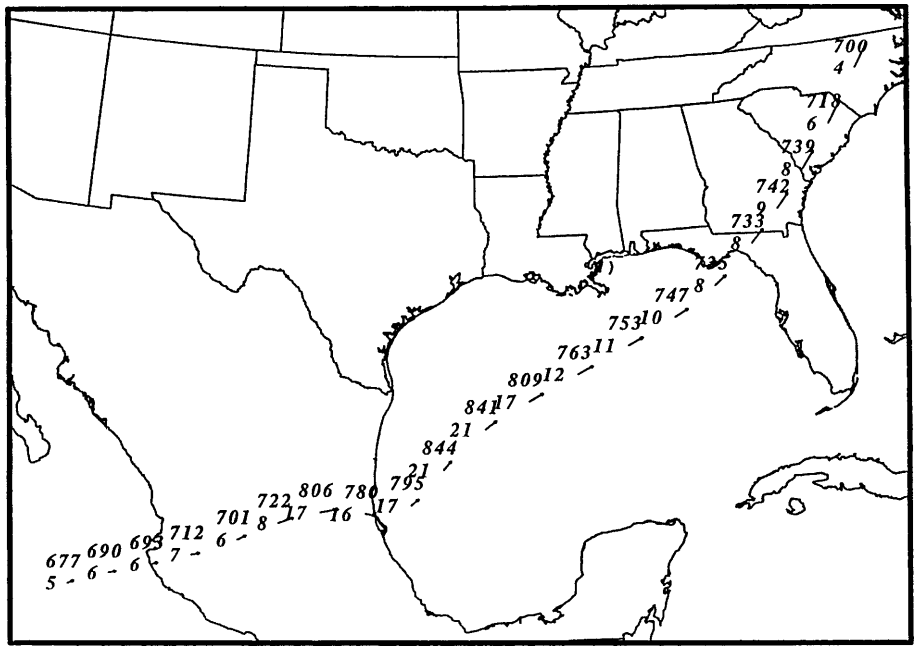

a

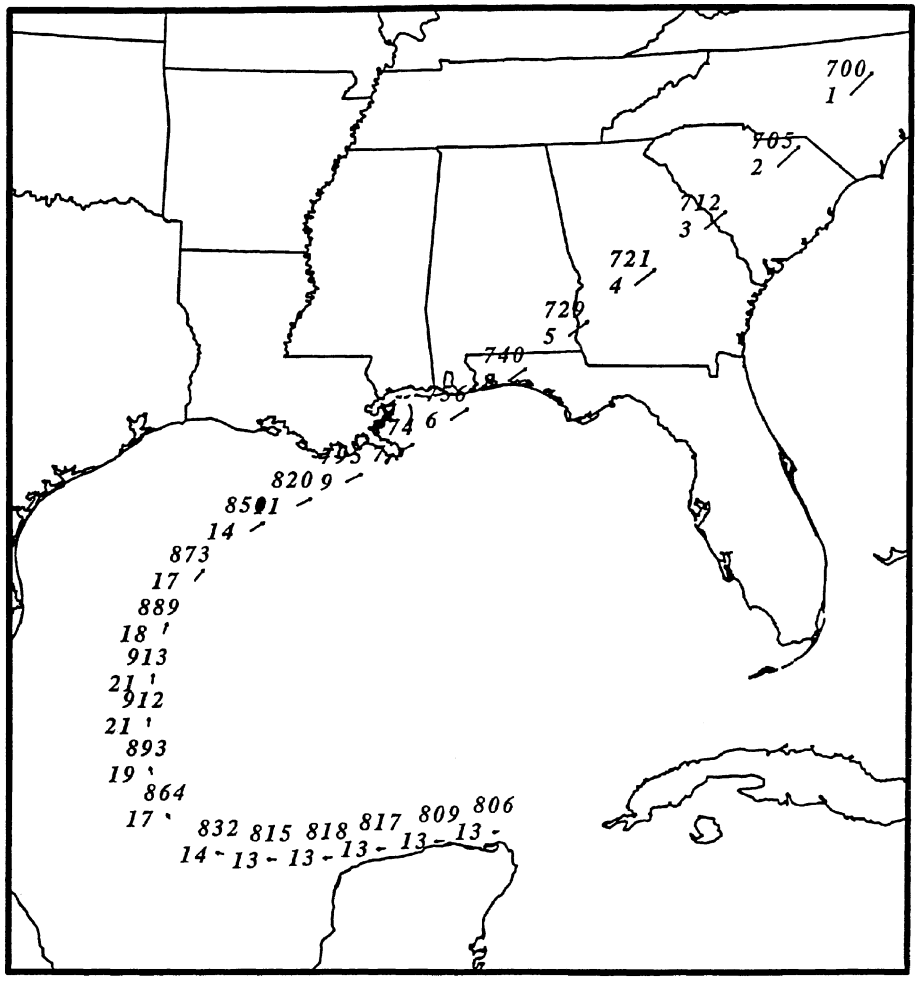

b

Fig. 7. Trajectories constructed from the 72 km simulations for parcels ending at 700 hPa over RDU. Station plots contain pressure (hPa) and temperature (C). Displayed wind vectors depict total wind (ms^{-1}). Parcels initialized at **a** 0600 UTC 28 and ended at 0900 UTC 25 November 1988, and **b** 2100 UTC 22 and ended at 1800 UTC 25 January 1990

Fig. 7. Continued. Valid at 2100 UTC 22 January 1990 to 1800 UTC 25 January 1990

In addition, three-dimensional parcel trajectories used throughout these papers are derived from a Mesoscale Atmospheric Simulation System Trajectory (MASSTRAJ) software package (Rozumalski, 1997). MASSTRAJ uses model-simulated mass and momentum fields to retrace or forecast the path of an air parcel.

4. Airmass origin: 72 hour back trajectories

Three-dimensional parcel trajectories are constructed from the 72 km and 72 h simulations to identify the airmass origin. Parcels end over central NC at the time of the event and the expected time of the non-event. In the event case, there are three airstreams flowing into RDU. The upper-level flow (not shown) originates suthwest of the Baja of California. The mid-level flow (Fig. 7a) originates near Guadalajara. The low-level flow (not shown) originates near the Cayman Islands. In the non-event case there are two flows into RDU. The upper- and low-level flows (not shown) originate from the southwestern US. The mid-level flow (Fig. 7b) originates in the Mexican Gulf.

The mid-level trajectories highlight an important difference between the cases (in the event case, the movement of warm air off the Mexican plateau). The event case 700 mb air parcel originates off Guadalajara at 677 mb and moves over the Sierra Madre Orientals, descends (warming by adiabatic compression), moves over the Gulf, and finally ascends toward RDU (Fig. 7a). When it arrives over central NC it is unseasonably warm (with a temperature of 4 °C). By contrast, the non-event case parcel originates near the Yucatan Peninsula, circles the Gulf and ascends over the southeast US to RDU (Fig. 7b). The air parcel is unseasonably warm; however, it is cooler than the event case.

In summary, in the event case, the upper- and mid-level airmasses originate over Mexico and the low-level airmass originates over the Gulf of Mexico. In contrast, the high pressure over Mexico dominates the non-event case flow; thus the upper-level air parcels travel across the southern US. The low- and mid-level airmasses originate over the Gulf of Mexico. It will be shown in the next section that the event case trajectories are dominated by the STJ.

5. Simulated jet development

5.1 Jet development of the event case

The numerical simulations depict strong subtropical jetogenesis over northern MX and TX during the 0000 and 1200 UTC 25 November 1988 time period (Fig. 8a, b). The area of jet development is associated with low- to middle-tropospheric cold advection over the Rocky Mountains leading to height falls (north) and height rises (south) above the surface warmed air on the leeside of the Mexican plateau. Thickness advection for the 700–300 hPa layer is ploted (Fig. 9). The jetogenesis is associated with the maximum differential thickness advection. Parcel trajectories through the jet streak verify the existence of the expected transverse ageostrophic circulations about the jet (Fig. 10a). Throughout the trajectory period, the jet core is located over TX (Fig. 10b, c). The parcel originates upstream of the developing jet, accelertes, ascends and deflects to the left when it enters the jet (thermally direct circulation). The parcel then decelerates, deflects to the right and descends when it exits the jet (thermally indirect circulation), which is consistent with an idealized jet streak (Keyser and Shapiro, 1986).

The STJ's entrance region creates integrated mass flux divergence over eastern MX and the southwestern Gulf. In response to the upper-level divergence, the 1470 and 1500 m isoheights (Fig. 11) move southward, which indicates height falls. The 12 to 18 h forecasts depict a low-level trough developing over eastern MX and the western Gulf. Also, the lower tropospheric flow accelerates towards the northeast over the open waters of the Gulf. At 0600 UTC on 25 November 1988 the low-level flow off the TX coast is from the southwest at $5-10\,\mathrm{ms}^{-1}$ (Fig. 11a) and by 1800 UTC on the 25th (Fig. 11b), the low-level flow is about $15\,\mathrm{ms}^{-1}$. Similarly, the 700 hPa level (not shown) offshore low-level flow increases from $5-10\,\mathrm{ms}^{-1}$ to $15-20\,\mathrm{ms}^{-1}$. The LLJ is a low-level response to the upper-tropospheric ageostrophic circulation and the low-level trough. The accelerating LLJ transports the hot air from the Mexican plateau region to the eastern Gulf of Mexico coastal states by 1200 UTC 26 November 1988. *It will be shown that this hot air then becomes available to produce a*

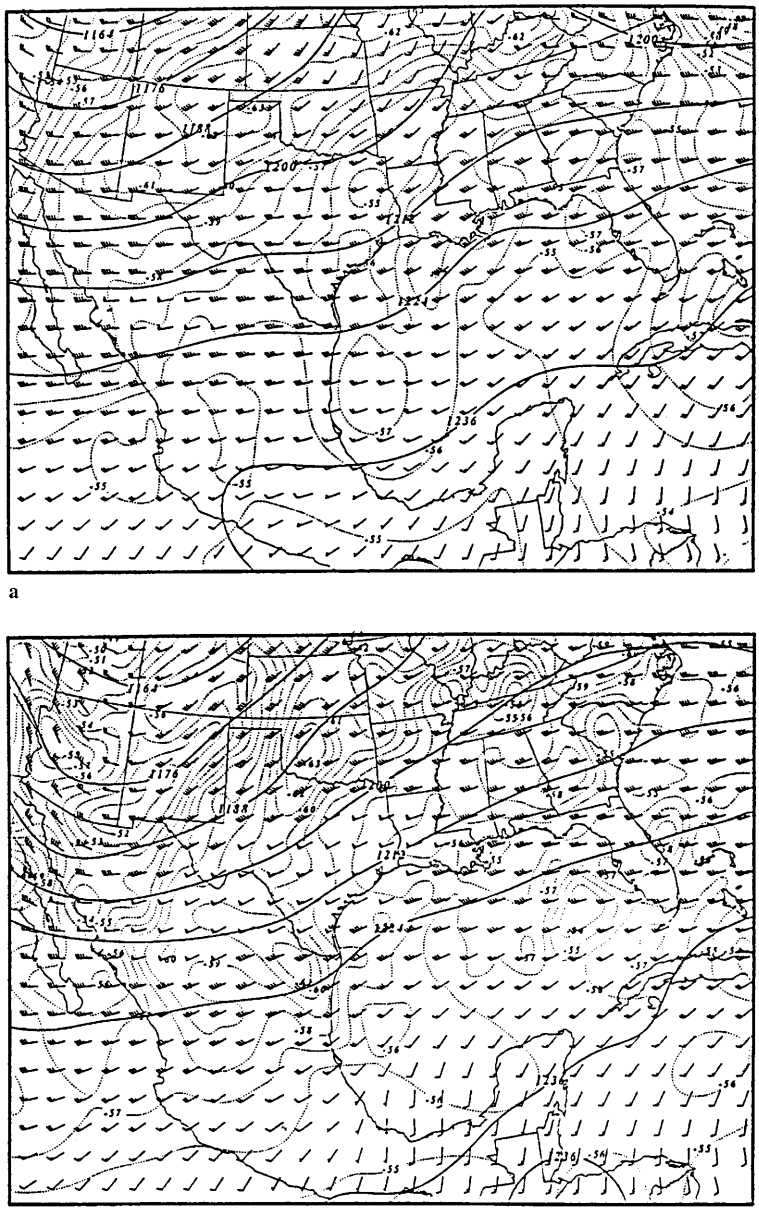

a

b

Fig. 8. Rawinsonde-derived analyses of 200 hPa wind vectors, temperature (dotted lines, C), and height (solid lines, dm) valid at **a** 0000 UTC 25, and **b** 1200 UC 25 November 1988

strong midlevel jet and convective instability during periods of geostrophic adjustment ahead of the polar front accompanying the PJ.

The significance of these dynamics can be best appreciated by examining a 72-hour backward trajectory (Fig. 12). The trajectory ends at 700 hPa, near RDU at 0000 UTC 28 November 1988. The parcel originates over the Mexican plateau, moves over the Gulf then takes a northeastward turn (point A) and begins to ascend in response to the increasing northward-directed LLJ (approximately 1800 UTC 25 November 1988). This signals the important role of the STJ in the transport of southern Mexican air towards the southeastern US.

In summary, the transverse ageostrophic circulation associated with the STJ removes mass from the air column, which creates ascent over the western Gulf of Mexico. Thus, a low-level trough and a LLJ develop over the western Gulf. The LLJ transports the hot air from the Mexican plateau to the southeast US.

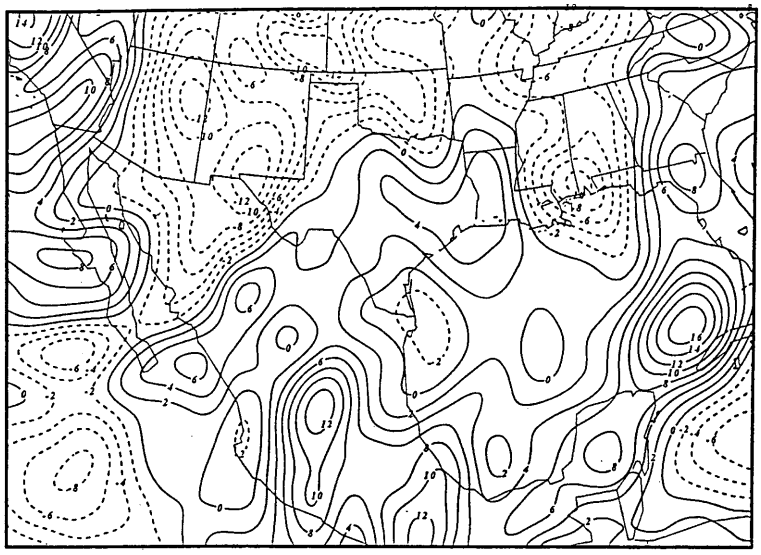

Fig. 9. MASS simulated, 24 km mesh, 700–300 hPa, 1 h thickness advection (solid lines denote positive value and dashed lines denote negative values, mh^{-1}) valid at 0600 UTC 25 November 1988

5.2 Jet development of the non-event case

There is strong PJ development (at 300 hPa) from 1800 UTC 22 to 18 UTC 23 January 1990 (Fig. 13a, b) over CO, KS, OK and MO. The PJ development also appears on the 200 hPa level. Again, the maximum jet development is associated with the maximum height falls and cold air advection. Throughout the entire period, there is an upper-level ridge over MX so the STJ does not develop over MX during the first 24 hours of the simulation; i.e., the wind speed varies by only $5\,ms^{-1}$.

We examine the 850 hPa level over the western Gulf of Mexico for any LLJ development. Figure 14a and b depict the 850 hPa level winds valid at 1800 UTC 22 and 1800 UTC 23 January 1990. At 1800 UTC 22 January 1990 the low-level flow is anticyclonic and is centered over the Gulf of Mexico. Over the southern US the flow is predominantly west to east with the exception of a small area of anticyclonic flow over a weak ridge over MS. By 1800 UTC on the 23rd, an upper-level jet begins to develop over CO, KS, OK, and MO (Fig. 13b). The thermally indirect circulation about the jet exit region induces a low-level flow from the south over AL and GA. In addition, the jet entrance region has a thermally direct circultion, which creates a low-level northerly flow over CO and NM with the winds accelerting to $10–15\,ms^{-1}$. A LLJ does not develop over the western Gulf of Mexico.

The difference between the cases in the jet development and synoptic situation is apparent when comparing the 850 hPa tempertures. Figure 15a and b depicts the 850 hPa temperature, pressure, and wind valid 1200 UTC 23 January 1990 and 0000 UTC 26 November 1988, respectively. Over the western Gulf, in the event case, the winds are from the southwest and the temperatures are 18 to 20 °C facilitating lee cyclogenesis. In the non-event the winds over the western Gulf coast are from the east and temperatures are 12 to 14 °C.

In summary, the non-event case has a different synoptic pattern, upper-level jet development and thus different low-level responses. At this time (48–72 hours before the expected event), the flow is zonal. A jet streak develops over northern TX stretching into MO (farther to the north than the event case). In the upper-levels, there is a weak ridge over MX. The ridge does not allow the STJ to move anywhere near the Gulf of Mexico inhibiting any LLJ development and the transport of the hot air from over the Mexican plateau towards the US Gulf Coast. Without the hot Mexican air over the southeastern US, the mid-level, cross-stream height gradient is weaker so the midlevel jet does not develop above the warm moist tropical air.

6. Potential vorticity

In this study, we investigate low-level *PV* production (Eq. 2), which is largely the product of diabatic processes normally considered small and neglected. We investigate the origins and

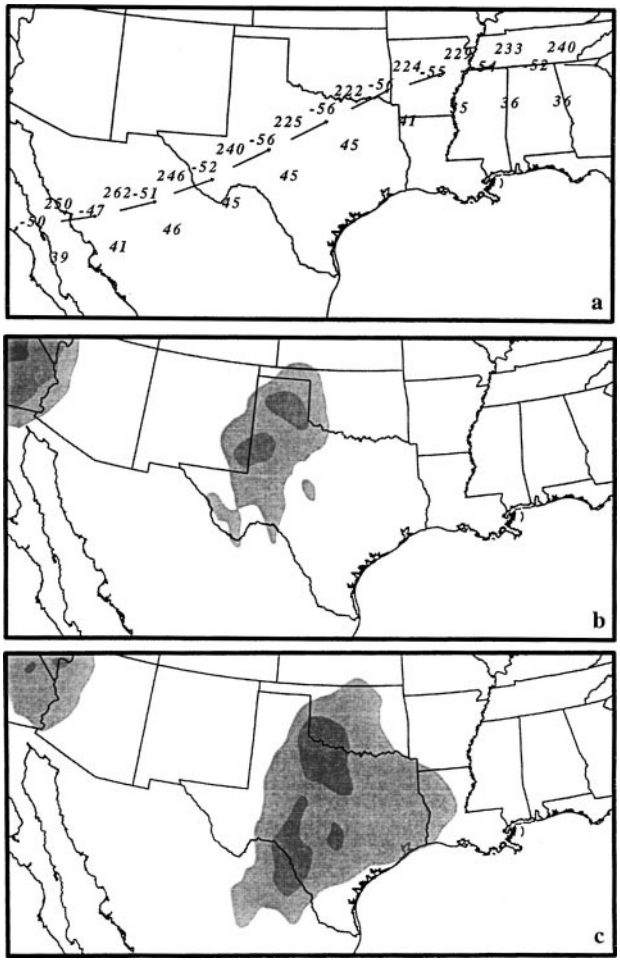

Fig. 10. MASS simulated, 24 km mesh **a** trajectory initialized at 0400 UTC 25 and ended at 0000 UTC 26 November 1988. Station plots contain pressure (hPa), temperature (C), and total wind speed (ms^{-1}). Displayed wind vectors depict total wind; **b** 250 hPa isotachs (shaded at intervals of 5 for speeds greater than $50\,ms^{-1}$) valid at 1500 UTC 26, and **c** 250 hPa isotachs (shaded at intervals of 5 for speeds greater than $50\,ms^{-1}$) valid at 2100 UTC 26 November 1988

transport of low-level *PV* because low-level *PV* is related to surface mesolow development and severe weather.

6.1. Origins of low-level potential vorticity 72 hours before event and non-event

For the event case, we examine the origins of the low-level *PV* maximum ending over central NC at the time of the tornado outbreak. Figure 16 depicts the 900 hPa *PV* maxima every 12 hours for the 72 hours before the event and non-event. In the event case (Fig. 16a–e), the *PV* maximum starts over the TX coast (just west of Houston) and moves east. When the maximum reaches the Alabama Gulf coast it turns to the northeast and moves over the central NC at the time of the tornado. The non-event case (Fig. 16f–j) has several *PV* maxima originating near the TX/OK border and moving across central AR and TN. These *PV* maxima weaken over time. A final *PV* maximum develops over central MS (associated with convection) at 1200 UTC 25 January 1990 and tracks to the Appalachians. Figure 17 depicts the 72-hour path of the low-level *PV* maximum. The low-level *PV* is traced using the widely accepted 1 *PV* unit ($\times 10^{-6}\,K\,hPa^{-1}s^{-1}$) demarcating air of stratospheric origin (Reed, 1955; Whitaker et al., 1988). The low-level *PV* maximum over central NC traces back to an area south of BRO. At the onset of the simulations (0600 UTC 25 November 1988) *PV* maxima are in the lee of the mountains over two areas: near Monterrey, MX (MMTY) and near DRT. The *PV* maximum near MMTY moves northeastward over Corpus Christi, TX (CRP) where it moves in close proximity to another *PV* maximum that formed near DRT. Parcel trajectories confirm the relative strength and movement of the *PV* maxima. The *PV* maximum originating near BRO is the dominant *PV* maximum.

We also examine the origins of the low-level *PV* maxima for the non-event case (Fig. 16f–j). There is a low-level *PV* maximum over the Appalachians, but not over central NC. The *PV* maximum traces back 21 hours into northern MS, then weakens until the track is not definable. Also, several *PV* maxima move east from the lee side of the Rocky Mountains across OK, AR and TN to the Appalachians. The 72-hour low-level *PV* maximum tracks are depicted in Fig. 17.

In summary, there are two significant differences between these cases. First, the event case *PV* maximum is a coherent and traceable entity over 72 hours. In the non-event case *PV* maximum is not a coherent entity. Second, the non-event case *PV* maximum appears to originate over the Rocky Mountains in CO. In the event case, the low-level *PV* maximum originates much farther to the south, over MX.

6.2 Generation of low-level potential vorticity 72 hours before event and non-event

We investigate the origins of the low-level *PV* south of BRO. A mountain wave exists after

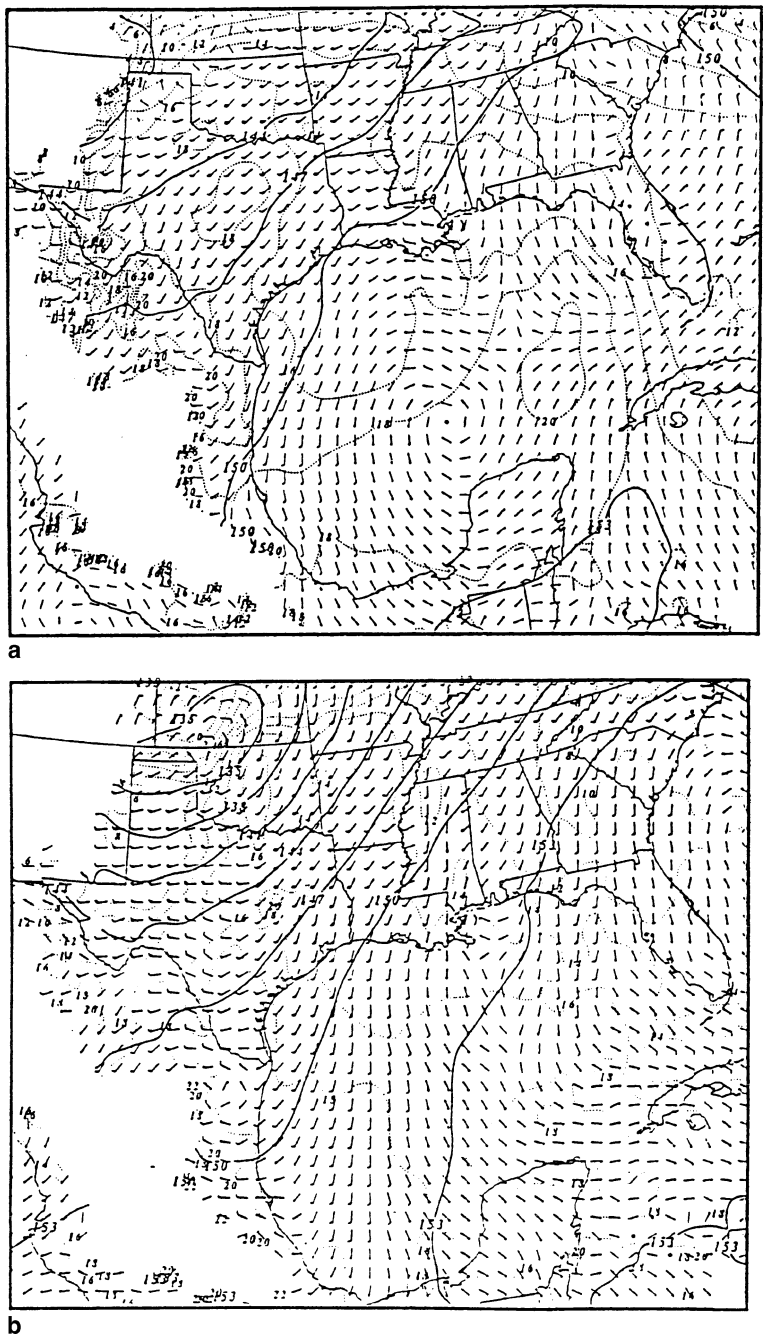

Fig. 11. MASS simulated, 24 km mesh, 850 hPa wind vectors, temperature (dotted lines, C), and height (solid lines, dm) valid at **a** 0600 UTC, and **b** 1800 UTC 25 November 1988

0600 UTC 25 November 1988 on the east side of the Sierra Madre Mountains (Fig. 18) evident in the low-level folding of the isentropes. Also, the Froude number over the Mexican plateau (upstream) was 1.03, which belongs to a flow regime conductive to producing strong downslope winds (Lin and Wang, 1996). The waves generated in the lee of the Sierra Madre mountains (wave breaking region) transport *PV* to the low-levels. The 0.5 (*PV* units) contour extended from the 500–600 hPa level over the mountains to the 900 hPa level along the coast.

The mid-level *PV* maximum is transported down the mountains but the next question is where does the mid-level *PV* originate. AT 1500 UTC 24 November 1988 (Fig. 19) there is a large upper-level *PV* maximum (> 4.5 *PV* units at 200 hPa) over TX and northern MX. The 1 *PV* unit

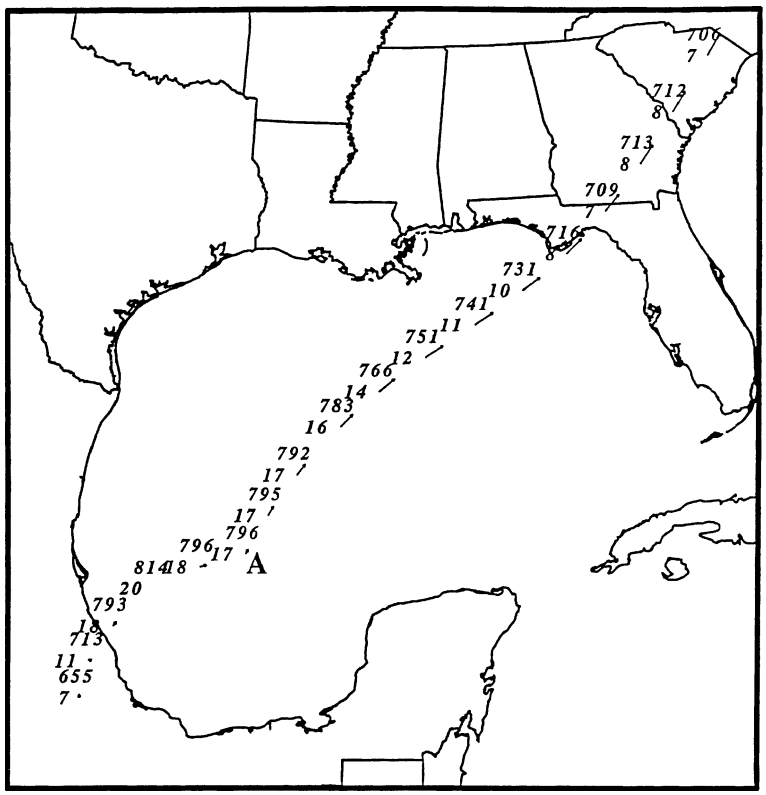

Fig. 12. Trajectory constructed from the 72 km mesh MASS simulation initialized at 0000 UTC 25 and ended on 0000 UTC 28 November 1988. Station plots contain pressure (hPa), temperature (C), and displayed wind vectors depict total wind

contour extended as far south as the southern tip of the Baja of California. As a STJ streak moves eastward over the west coast of MX its exit region and associated thermally indirect ageostrophic circulation (indicated by the ageostrophic wind directed to the right of the stream) approaches the upper-level *PV* maximum. Figure 20 (valid 1800 UTC 24 November 1988) is a cross section extending across the STJ exit region and the Mexican plateau depicting the thermally indirect ageostrophic circulation associated with the STJ streak. The thermally indirect ageostrophic circulation creates sinking (A in Fig. 20) in the right exit region of the jet streak (over the Mexican plateau) facilitating the downward transport of *PV* and ascent in the left exit region (B in Fig. 20). Descent in the right exit region of the jet streak core transports a lobe of upper-level PV down to the middle troposphere (500–600 hPa). This situation is considerably different from the isolated jet/front system used by Danielsen (1968) to develop his conceptual model of the downward transport of *PV* in the left entrance region of the jet. Danielsen concluded the greatest production of *PV* is associated with strong static stability found in the left jet entrance region where sinking was also occurring so downward transport of *PV* would mainly occur in that area. The conceptual model did not include the interaction of several jet streaks. In the event case, there are two jet streaks within the STJ; the first jet streak (located over TX and the Gulf Coast States) facilitates *PV* production and transports the *PV* southward. Then the second STJ streak and its associated thermally indirect circulation transports the *PV* to the mid-levels over the Mexican plateau. The downward transport of *PV* is another way the STJ is critical for the future development of severe weather over the southeast US.

The *PV* is transported to the mid-levels until approxiately 2000 UTC 24 November 1988. At the same time, there is substantial heating over the Mexican plateau. By 0000 UTC 25 November 1988 (Fig. 21), there is a deep and warm dry adiabatic layer (potential temperature of 310 K

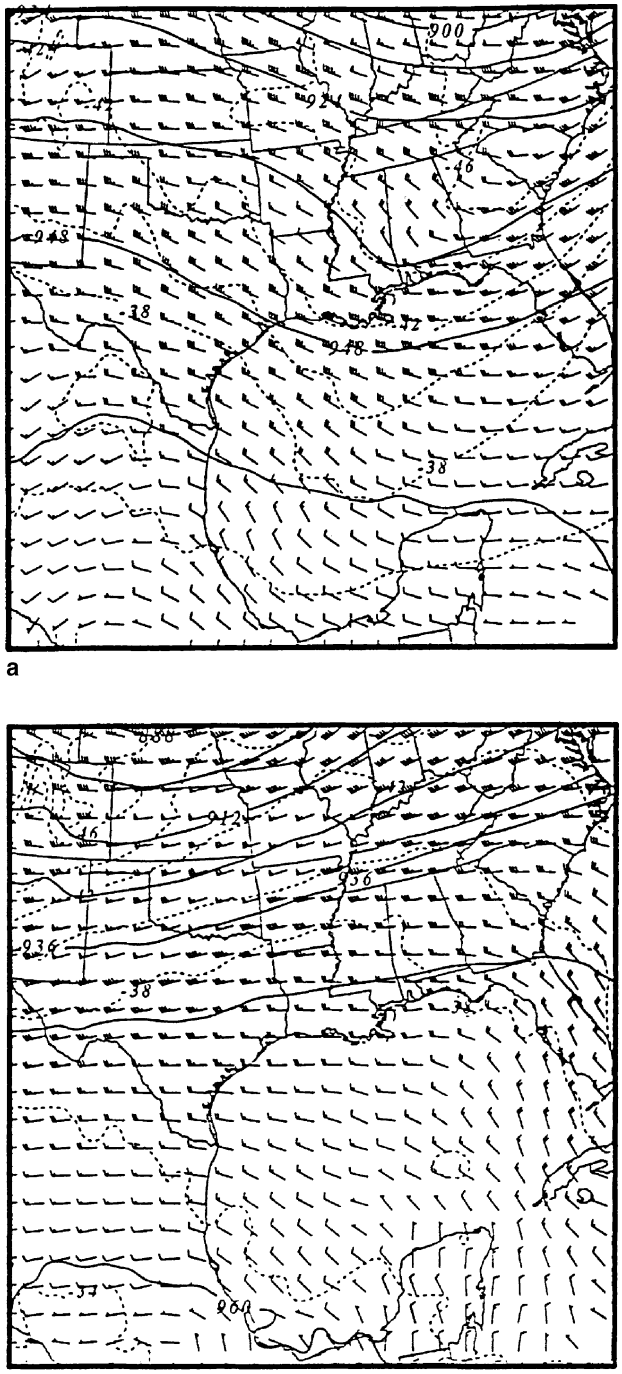

a

b

Fig. 13. MASS simulated, 24 km mesh, 300 hPa wind vectors, temperature (dashed lines, C), and height (solid lines, dm) valid at **a** 1800 UTC 22 January 1990, and **b** 1800 UTC 23 January 1990

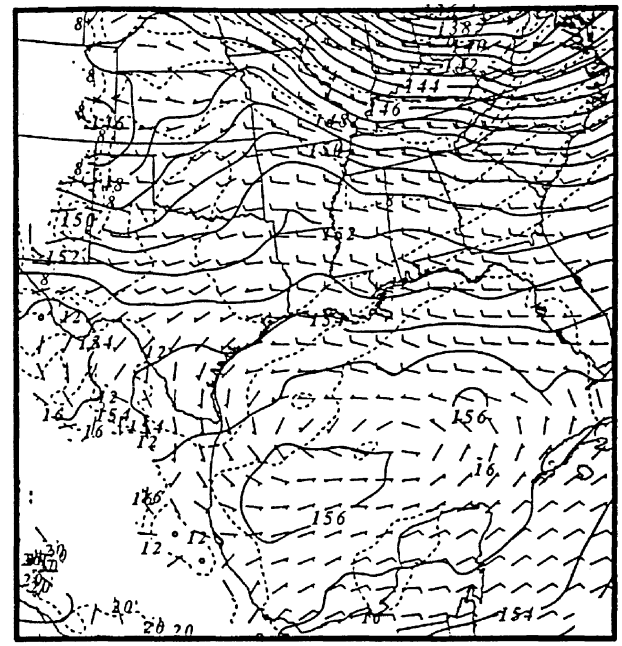

a

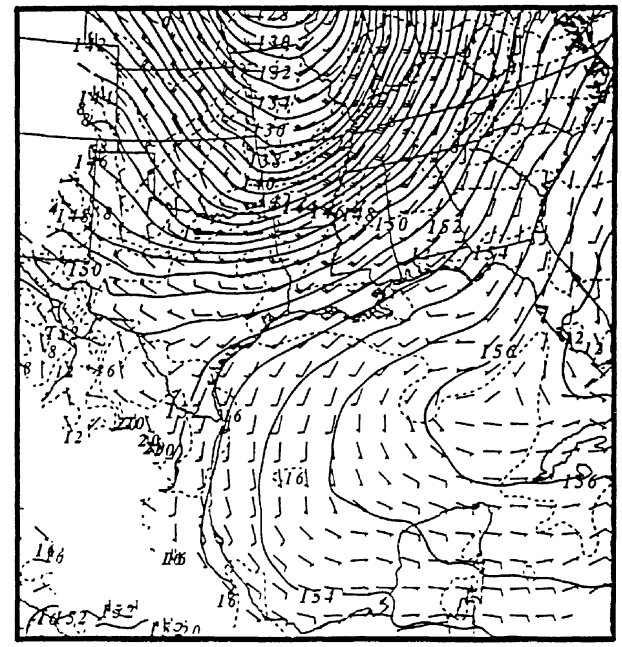

b

Fig. 14. MASS simulated, 24 km mesh, 850 hPa wind vectors, temperature (dashed lines, C), and height (solid lines, dm) valid at **a** 1800 UTC 22 January 1990, and **b** 1800 UTC 23 January 1990

up to $\sim$ 650 hPa) over MX, which is being forced by large surface sensible heat fluxes resulting from clear skies, minimal soil moisture and arid conditions. We will refer to the area within the box as the *PV* generation area (Fig. 17). By 2100 UTC, a mountain-plains solenoid (MPS) (Tripoli and Cotton, 1989) produces a well mixed, elevated boundary layer. In the eastern half of the *PV* generation area, strong ascent occurs in the low levels and descent

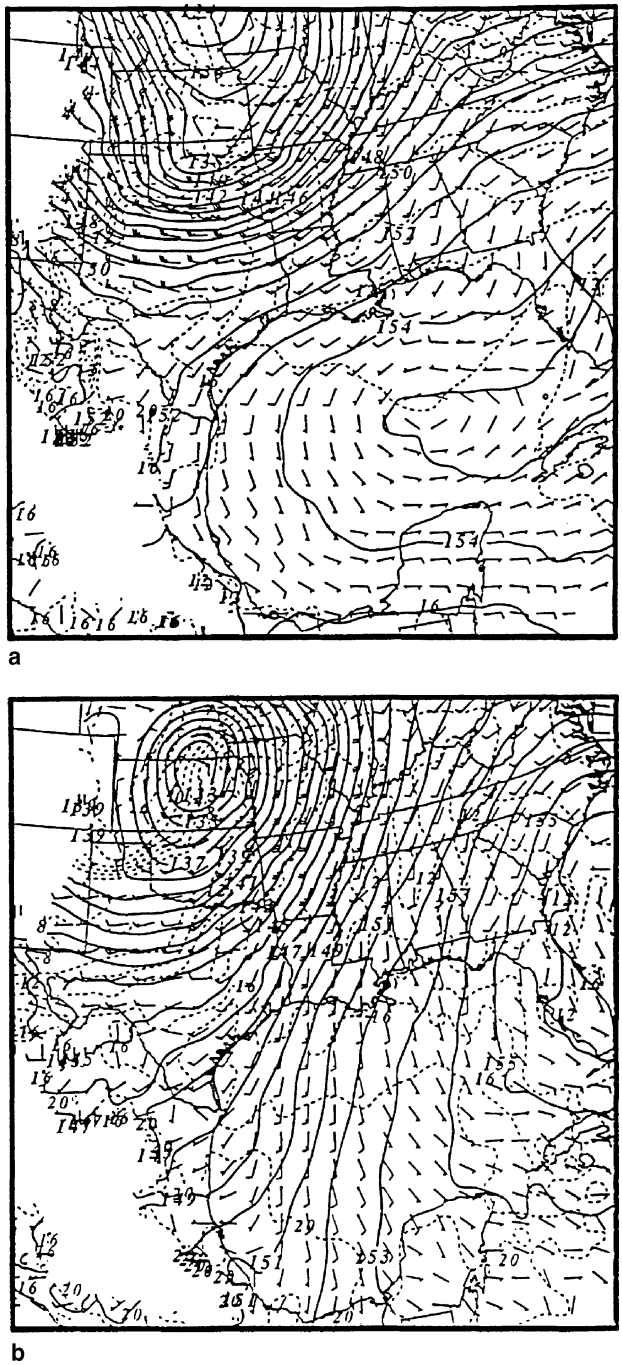

Fig. 15. MASS simulated, 24 km mesh, 850 hPa wind vectors, temperature (dashed lines, C), and height (solid lines, dm) valid at **a** 1200 UTC 23 January 1990, and **b** 0000 UTC 26 November 1988

occurs in the mid and upper levels. At 0100 UTC 25 November 1988 (Fig. 22) these two ageostrophic circulations create an area of vertical convergence in the 500–600 hPa layer over the eastern half of the *PV*-generation area (Fig. 17). This convergence perturbs the potential temperature field, increases the thermal gradient (static stability) and generates *PV* in the 500–600 hPa layer. The relative contribution of each term in the *PV* (Eq. 2) is evaluated at 0100 UTC about the 625 mb level in the *PV* generation area in a manor analogous to Kaplan and Karyampudi (1992b). Data used in the calculations are taken from parcel trajectory output with the exception of the gradient field, which is derived using a centered finite differencing scheme calculated from trajectories surrounding the center trajectory point. Term 1 dominates the production of *PV* (contributing 78%) by the dramatic increase in static stability associated with the intense diabatically-forced thermal gradient (and vertical frontogenesis) above the dry adiabatic layer. Surface sensible heating is the main contribution to the diabatically-forced thermal layer. This mid-level *PV* maximum moves eastward and by 0600 UTC it is over the Sierra Madre Orientals. Later, during the 0600–1200 UTC nocturnal period, a hydrostatic mountain wave develops in the lee of the mountains (Fig. 18) facilitating the downward transport of the midlevel *PV* generated earlier. Model-generated soundings indicate an inversion develops due to radiational cooling over the coastal area in the early morning hours. Thus, the low-level *PV* moves down the lee of the mountains and increases due to strong static stability in the presence of nocturnal surface cooling.

For the non-event case we again examine the flow on the east side of the Sierra Madre Mountains near BRO (Fig. 23). Throughout the simulations there were no low-, mid-, or upper-level *PV* maxima over the coastal region. *In the non-event case, the low-level wind field over the Gulf of Mexico was from the east thus no mountain waves developed near BRO. Also, there was not a STJ to facilitate the downward transport of mid- or upper-level PV*. Additionally, cross sections depict very little daytime heating over the Mexican plateau (Fig. 24). The easterly low-level wind advects moisture rich air over the Mexican plateau producing low-level clouds thus minimizing the solar radiation and surface warming. The advection of relatively warm, moist air off the Gulf reduces the intensity of the nocturnal inversion because of reduced radiational cooling, hence, less *PV* production

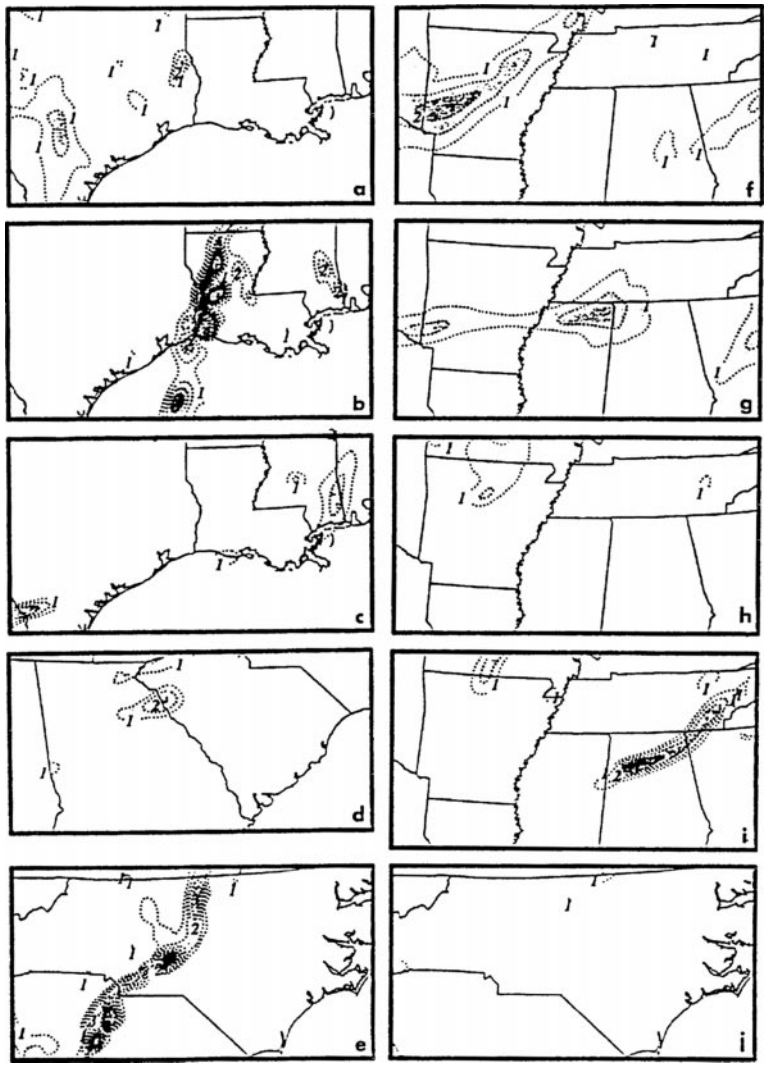

Fig. 16. MASS simulated, 24 km mesh 900 hPa PV (shaded greater than 1 PV unit by 0.5) valid at **a** 0600 UTC 26, **b** 1800 UTC 26, **c** 0600 UTC 27, **d** 1800 UTC 27, **e** 0600 UTC 28 November 1988, **f** 1800 UTC 23, **g** 0600 UTC 24, **h** 1800 UTC 24, **i** 0600 UTC 25, and **j** 0000 UTC 26 January 1990

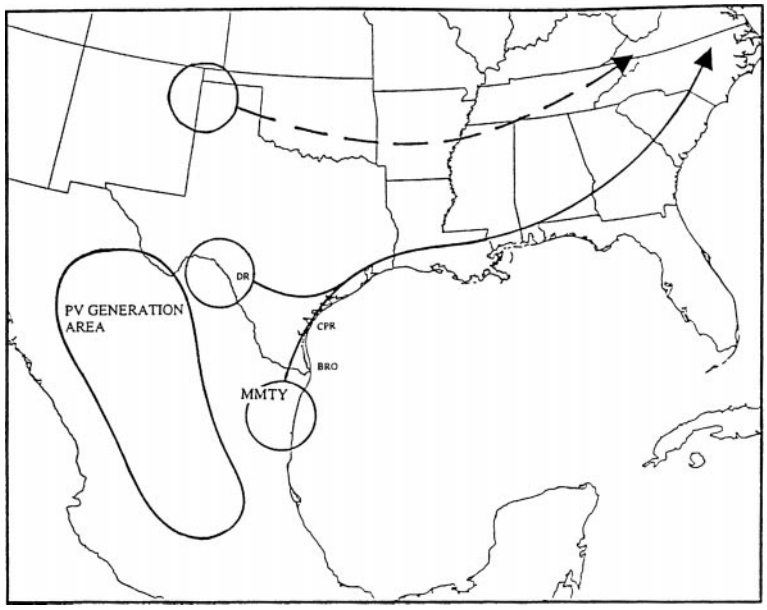

Fig. 17. Depiction of 900 hPa PV maximum track using 24 km mesh MASS simulation data, solid line is event case and dashed line is non-event case

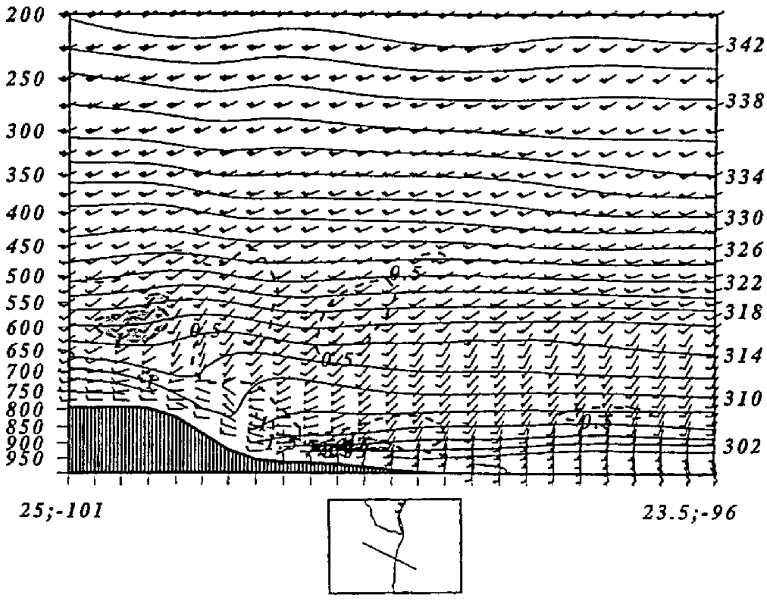

Fig. 18. MASS simulated, 24 km mesh, cross section extending from 25N, 101W to 23.5N, 96W. Includes wind vectors, θ (solid lines, K), and PV (dashed lines, contoured by 0.5 and shaded greater than 1 PV unit) valid at 1200 UTC 25 November 1988

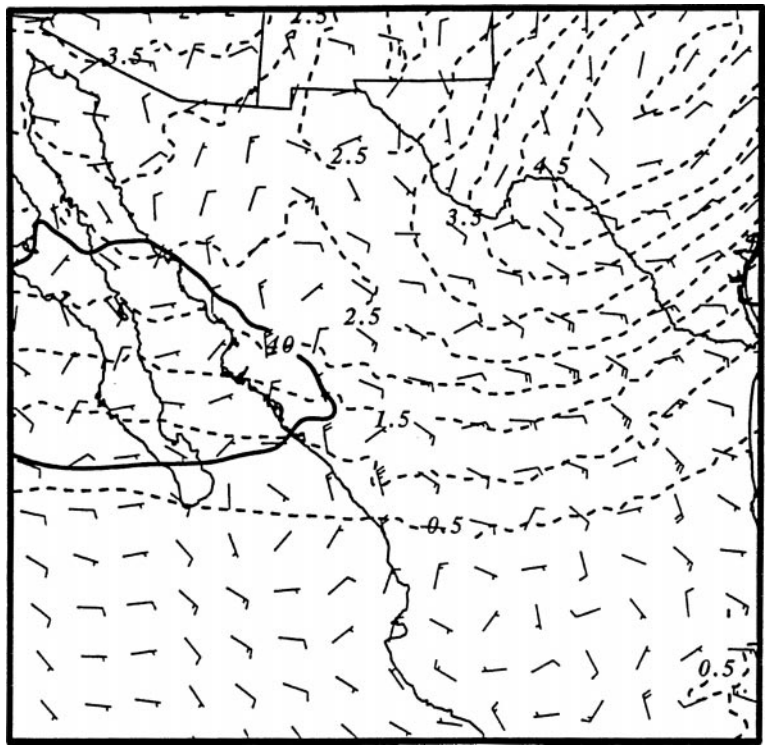

Fig. 19. MASS simulated, 24 km mesh, 200 hPa PV (dashed line, contoured by 0.5 PV units), wind speed (solid line, contoured at 40 ms^{-1}) and ageostrophic wind vectors valid at 1500 UTC 24 November 1988

occurs as the stability is weaker than in the event case. Throughout the evening, a shallow surface inversion develops over the mountains increasing low-level PV over this region due to the increasing static stability. Also, we examine the PV maximum east of the Rocky Mountains over northern TX and OK. The PJ induces waves in the lee of the mountains, which transports PV downward.

Next, we evaluate the relative contribution of each term in Eq. 2 as the parcel descends the leeward mountain slope. In the event case, the

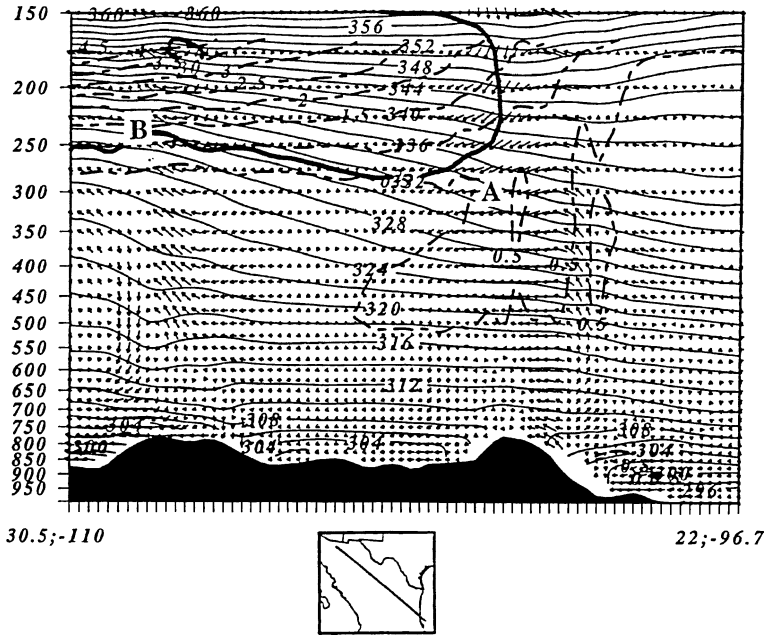

Fig. 20. MASS simulated, 24 km mesh, cross section extending from 30.5N, 110W to 22N, 96.7W. Includes ageostrophic wind vectors, θ (solid line, K), wind speed (thick solid line, contoured at 25 and 30 ms^{-1}) and PV (dashed lines, contoured by 0.5 PV unit) valid at 1800 UTC 24 November 1988

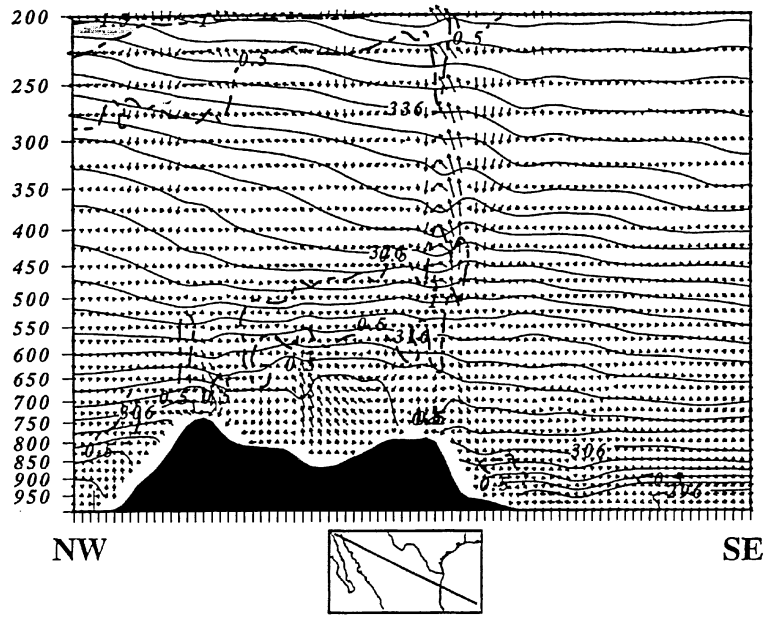

Fig. 21. MASS simulated, 24 km mesh, cross section extending from 26.5N, 110W to 22.2N, 92.5W. Includes ageostrophic wind vectors, θ (solid lines, K), and PV (dashed lines, contoured by 0.5 and shaded greater than 1 PV unit) valid at 0000 UTC 25 November 1988

total PV increased 412%, from 0.7665 (PV units) to 3.159 (PV units). Term one contributes 30.6% to the producton of PV by the change in static stability associated with the developing low-level radiation inversion over the coastal region. Also, vorticity increases due to vortex tube stretching as the air volume advects down the mountains. Term two contributes 31.9% to the change in PV resulting from horizontal gradients of diabatic heating within regions of wind covariances. The 910 hPa PV maxima is within the inversion hence it is affected by friction. Term three contributes 37.5% to the production of PV resulting from the tilting of the horizontal component of vorticity into the vertical through horizontal diabatic heating. The low-level

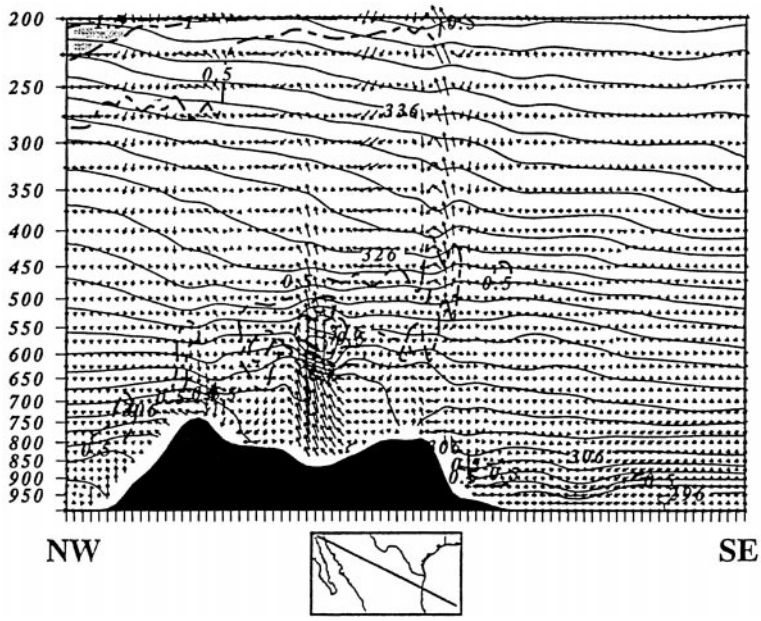

Fig. 22. MASS simulated, 24 km mesh, cross section extending from 26.5N, 110W to 22.2N, 92.5W. Includes ageostrophic wind vectors, θ (solid lines, K), and PV (dashed lines, contoured by 0.5 and shaded greater than 1 PV unit) valid at 0100 UTC 25 November 1988

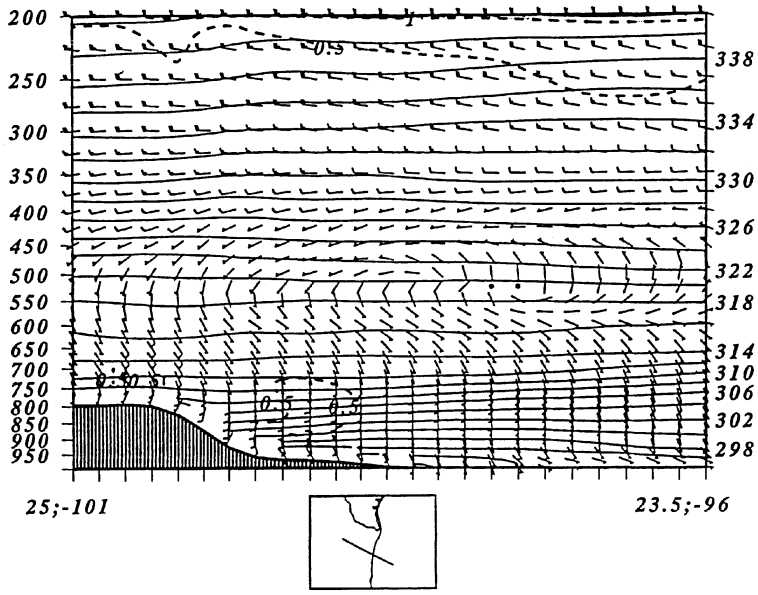

Fig. 23. MASS simulated, 24 km mesh, cross section extending from 25N, 110W to 23.5N, 96W. Includes wind vectors, θ (solid lines, K), and PV (dashed lines, contoured by 0.5 and shaded greater than 1 PV unit) valid at 0900 UTC 23 January 1990

vertical wind shear and vertical potential temperature gradient advect down the mountains (and is tilted) generating PV. The diabatic forcing mechanisms in the PV equation (Eq. 2) that are typically neglected are very important in the low-level generation of PV.

In the non-event case, the parcel trajectory is different from the event case ascending the Sierra Madre Orientals then circling (clockwise) the mountains. As the parcel ascends the lee slope of the Sierra Madre Mountains, the total PV decreases from 0.273 PV units at 982 hPa to 0.173 PV units at 788 hPa. The decrease of low-level PV is due to a production of anticyclonic vorticity. Our calculations from model output indicate that term one produces 69% of the total anticyclonic vorticity. Term one represents the production of anticyclonic PV by vortex tube

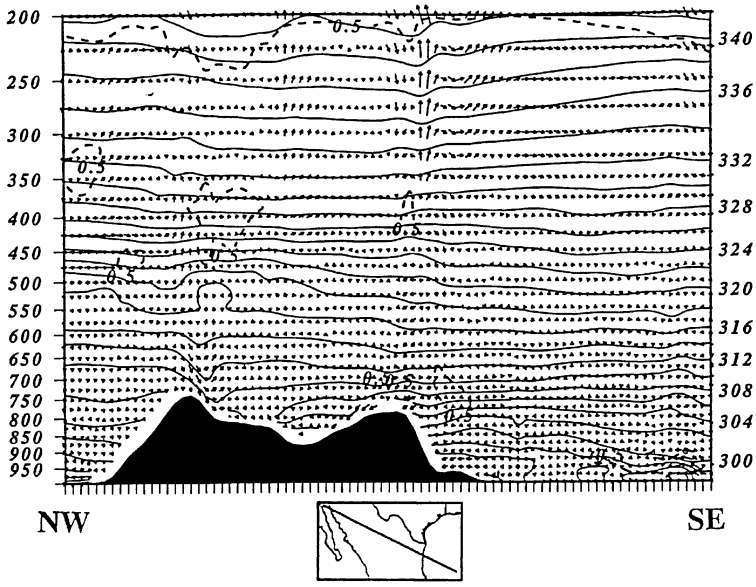

Fig. 24. MASS simulated, 24 km mesh, cross section extending from 26.5N, 110W to 22.2N, 92.5W. Includes ageostrophic wind vectors, θ (solid lines, K), and PV (dashed lines, contoured by 0.5 and shaded greater than 1 PV unit) valid at 0000 UTC 23 January 1990

contracting as the air volume moves up the mountains. Term two contributes 13.8% to the production of anticyclonic PV resulting from horizontal gradients of diabatic heating within regions of wind covariances. The frictional component consists of effects from barotropic surface drag and the baroclinic effect of mixing. Term three represents a smaller amount (17.2%) of anticyclonic PV production as the low-level vertical wind shear and vertical potential temperature gradient are advected up the mountains. Here, the synoptic flow is transporting the parcels in a clockwise direction over the mountains (rightward-directed KE). We hypothesis that the large scale mixing is bringing down the rightward directed momentum overwhelming the effects of surface drag and producing anticyclonic PV.

6.3 Maintenance of low-level potential vorticity

We investigate the transport and maintenance of the low-level PV as it moves north along the TX coast. First, we examine the possibility that the continuous downward transport of the upper-level PV maintains the low-level PV. We produce numerous cross sections through the low-level PV maximum as it propagates up the TX coast. Throughout this period, there is no downward transport of the upper-level PV. Supporting the idea that the PV is generated and maintained in the low levels.

We examine other potential energy sources (wind shear gradient, potential temperature gradient, and surface convergence) and their relationship to low-level PV. These energy sources all act to produce and/or maintain PV via Term 3 in Eq. (2). The figures valid 1200 UTC on 25 November 1988, depict: 900 hPa PV and the gradient of the magnitude of wind shear over the 925 to 850 hPa layer (Fig. 25a), 900 hPa PV and surface streamlines (Fig. 25b), and 900 hPa PV and surface potential temperature (Fig. 25c). Each PV maximum (>1 PV unit) is associated with a strong vertical and horizontal wind shear gradient, localized areas of strong gradients of potential temperature, and a convergence area. The low-level PV maxima are associated with these energy sources throughout the simulation. In addition, the strength of the vertical and horizontal wind shear associated with the LLJ is closely corelated to the low-level PV – as the shear weakens so does the PV. So, it appears a combination of strong vertical and horizontal wind shear, surface convergence and a thermal gradient are essential ingredients for the production or maintenance of low-level PV. Low-level vertical and horizontal wind shear

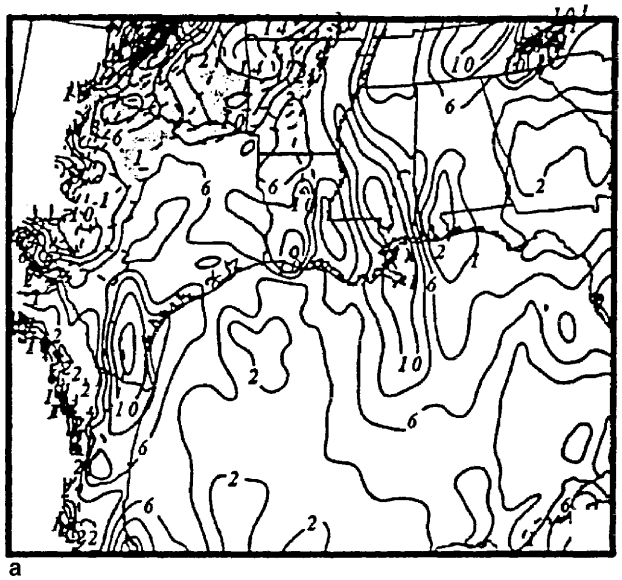

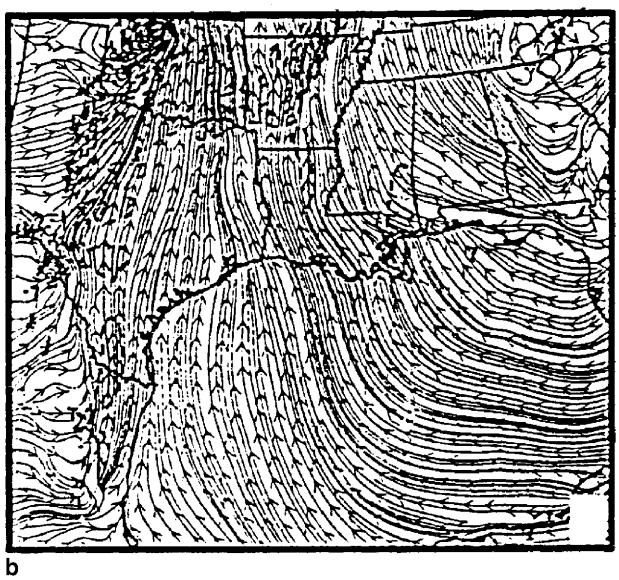

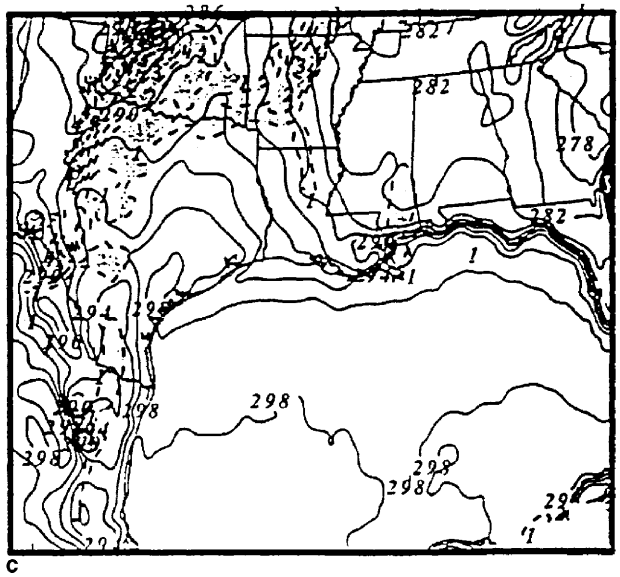

associated with the LLJ is the most likely transport and maintenance mechanism of *PV* since the LLJ is tied to the persistent STJ.

Next, we investigate the transport and maintenance of low-level *PV* for the non-event case. Depictions of the 900 hPa *PV* and the magnitude of wind shear, potential temperature gradient, and surface convergence show a different relationship than the event case. The depictions valid 0000 UTC on 23 January 1990 (Fig. 26a, b, c) have no significant areas of *PV*. Over GA, SC and NC there is strong vertical and horizontal wind shear. However, there is no significant convergence and a weak potential temperature gradient thus no low-level *PV* maximum.

6.4. Lagrangian investigation of low-level potential vorticity

In the final *PV* analysis of the event case, we switch to a Lagrangian frame of reference. We locate the *PV* maximum south of BRO and send a parcel through that area at 0600 UTC 25 November 1988. The parcel originates over the Sierra Madre Mountains at 0300 UTC, descends over the coastal area, moves northward, moves in proximity with another low-level *PV* maximum (originating from the mountains near DRT) and continues to move northeastward to LA (Fig. 27). The *PV* maximum originating over MX is the dominant feature. In this trajectory, the parcel's motion vector is almost exactly the same as the *PV* maximum's vector so the parcel's movement and values listed in Table 2 can be considered a volume encompassing the *PV* maximum. The *PV* associated with the parcel increased as it descended to the 910 mb level due to static stability, vortex tube stretching, tilting, and frictional effects. As the *PV* maximum (parcel) moves northward along the coast it is maintained by convergence, a thermal gradient, and strong low-level wind shear associated wih the LLJ. As the LLJ's shear field weakens with time so does the *PV* maximum. At approximately 0300 UTC

Fig. 25. MASS simulated, 24 km mesh, valid at 1200 UTC 25 November 1988 of *PV* (contoured (dashed lines) and shaded greater than 1 *PV* unit) and **a** magnitude of shear (solid lines, ms^{-1}) over the 925 to 850 hPa layer, **b** surface streamlines, and **c** surface theta (solid lines, K)

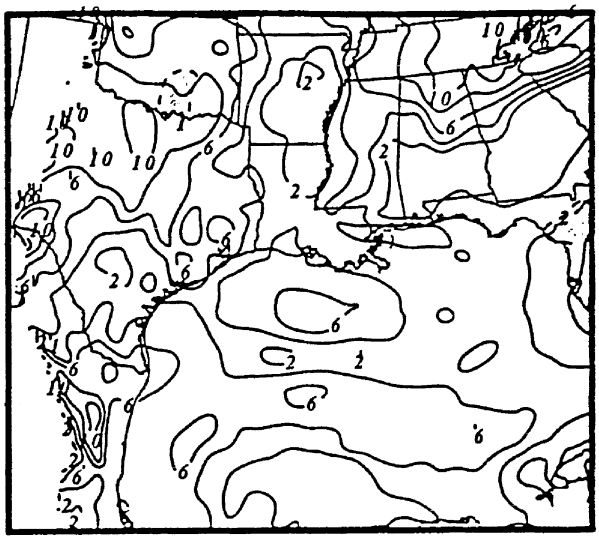

a

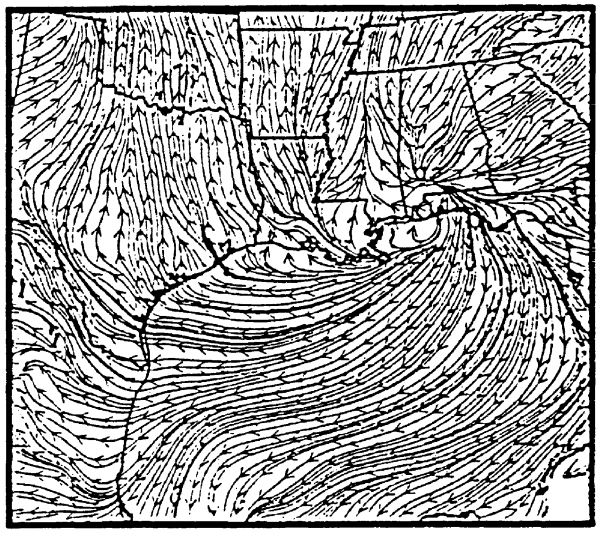

b

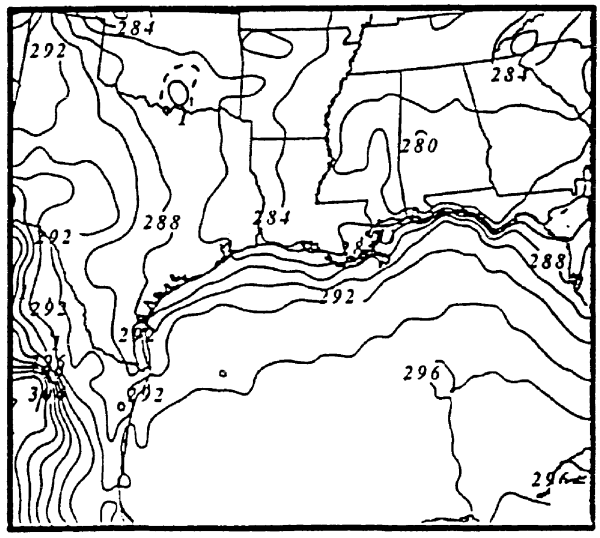

c

26 November 1988, the parcel enters an area of convection in eastern TX; consequently, the *PV* maximum increases from latent heat energy. Figure 27 depicts the parcel trajectory and 900 hPa latent heating ($^{\circ}\mathrm{Ch}^{-1}$) at 0400 UTC 26 November 1988. The greatest *PV* increase (from 0.8989 to 1.705 *PV* units) occurs when the parcel moves through a latent heating maximum ($> 40^{\circ}\mathrm{Ch}^{-1}$) at 0400 UTC. Sensible heating is aso examind, but is negligible (maximum value of $0.11\,\mathrm{Ch}^{-1}$). So, the low-level *PV* increase is directly related to latent heating.

In summary, south of BRO, the *PV* is initially transported downward to the mid-levels by the ageostrophic circulation associated with the STJ, maintained by the mountain-plains solenoid, then transported to the low-levels by an ensemble of mountain waves. Also, diabatic effects accompanying increased static stability, vortex tube stretching, tilting and frictional effects generate *PV*. The *PV* is transported by the LLJ and maintained by low-level wind shear and latent heating. The low-level *PV* maximum originates east of the mountains near BRO, moves northeast, follows the coastline along the Gulf States and up to RDU at the time of the tornado.

In the final *PV* analysis of the non-event case we again examine parcel trajectories. Parcels on the leeward side of the mountains all originate over the low coastal area of northeastern MX, ascend over the Sierra Madre Orientals then move clockwise back over MMTY some 24 hours later (Fig. 28, Table 4). The synoptic flow and parcel movement is very different from the event case. In the non-event case, the parcel ascends (cools) the leeward side of the Sierra Madre Mountains then descends (warms) over the MX plateau. In the lee of the mountains, there is little low-level *PV* most likely because the east to west flow does not facilitate the development of mountain waves or a surface inversion, which facilitates low-level *PV*. Over the parcel's path, there is no convection (latent heating) over the Mexican plateau. As the parcel

Fig. 26. MASS simulated, 24 km mesh, valid at 0000 UTC 23 January 1990 of 900 hPa *PV* (contoured (dashed lines) and shaded greater than 1 *PV* unit) and **a** magnitude of shear (ms^{-1}) over the 925 to 850 hPa layer, **b** surface streamlines, and **c** surface theta (K)

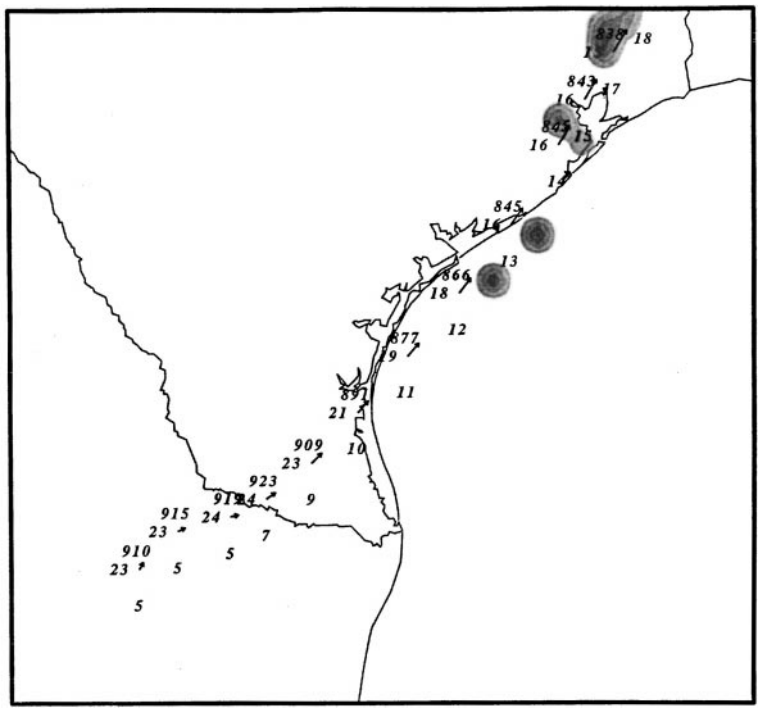

Fig. 27. MASS simulated, 24 km mesh, trajectory initialized at 0600 UTC 25 and ended at 0600 UTC 26 November 1988 plotted over latent heating due to convection (contoured by 10 Chr^{-1}) at 900 hPa. Station plots contain pressure (hPa), temperature (C), and total wind speed (ms^{-1}). Displayed wind vectors depict total wind

Table 2. Trajectory initiated at 0300 UTC 25 November 1988, passed through the 910 hPa PV maximum (25.7N, 99.8W) at 0600 UTC 25 November 1988 and ended at 0500 UTC 26 November 1988. Trajectory data shown here is every 2 hours and was derived from hourly data of a 24 km MASS simulation. The following abbreviations are defined: Latitude (LAT), Longitude (LON), Pressure (PRS), Temperature (TMP), and Potential Vorticity (PV).

Time (UTC)	LAT (°N)	LON (°W)	PRS (hPa)	TMP (°C)	PV (PV units)
25/0400	25.25	100.57	765.3	11.7	.7665
25/0600	25.33	100	910	23.8	3.159
25/0800	25.94	99.52	915.5	22.9	2.408
25/1000	26.09	99.2	914.6	23.3	2.131
25/1200	26.15	98.84	919.4	23.57	1.971
25/1400	26.3	98.48	922.6	23.8	1.695
25/1600	26.6	98.02	908.8	22.53	1.402
25/1800	27.05	97.53	890.6	20.82	1.094
25/2000	27.54	96.99	876.5	19.32	0.959
25/2200	28.09	96.41	866.1	18.1	0.8657
26/0000	28.67	95.82	844.8	16.36	0.8989
26/0200	29.37	95.24	844.6	16.17	1.0932
26/0400	30.16	94.57	837.9	15.27	1.705

moves across the Mexican plateau through the evening hours a weak radiation inversion develops, which increases the low-level stability generating small amounts of low-level *PV*. Weak daytime heating also acts to increase the low-level stability, which maintains the weak, low-level *PV*. The most significant aspect of the parcel trajectory is that the parcel and any associated *PV* remains over MX. Without the STJ and its associated LLJ the warm, *PV* rich air is not transported to the north. In summary, very weak, low-level *PV* is generated over the MX plateau; however, there is not a transport mechanism (LLJ) to move the *PV* over the US.

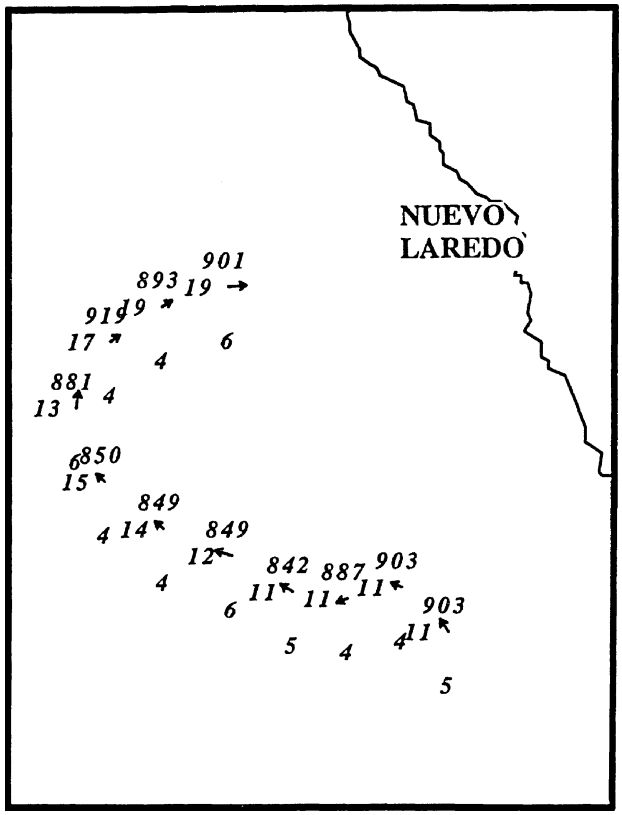

Fig. 28. MASS simulated, 24 km mesh, trajectory initialized at 1800 UTC 22 and ended at 1800 UTC 23 January 1990. Station plots contain pressure (mb), temperature (C), and total wind speed (ms^{-1}). Displayed wind vectors depict total wind

7. Conclusion

Observational analysis and mesoscale numerical simulations are in agreement concerning key dynamical processes which occurred over MX and the Gulf of Mexico 72 hours prior to the 1988 Raleigh, NC, tornado outbreak. Strong cold air advection over NM and northwestern TX intensified the height gradient (PGF) and, in turn, intensified the STJ streak over TX and MX. Initially, the STJ exit region and its associated transverse ageostrophic circulation created sinking over the Mexican plateau. Air was forced down the eastern side of the Sierra Madre Mountains, which warmed due to adiabatic (compressional) heating. Along with this warm air, a low-level trough of low pressure developed over the western Gulf of Mexico. The STJ right entrance region moved over the western Gulf of Mexico, which helped create upper-level divergence, upper-level mass removal and ascent in the air column. The low-level convergence, ascent throughout the levels and velocity divergence aloft helped develop the surface trough and the associated LLJ. This LLJ began the process to transport warm low-level air from the Mexican plateau to the Piedmont.

The non-event case had a different synoptic pattern. Seventy-two hours before the expected event, the upper-level flow was zonal over the US with a ridge over MX. A PJ developed over northern TX, OK and MO. The upper-level ridge prevented the development of a STJ over Mexico. During the early period, no transport

Table 3. Same as Table 2 except trajectory initiated at 1800 UTC 22 January 1990 and ended at 1800 UTC 23 January 1990.

Time (UTC)	LAT (°N)	LON (°W)	PRS (hPa)	TMP (°C)	PV (PV units)
22/1400	25.6	99.67	982.3	13.2	0.273
22/1600	25.6	99.91	970.8	13.1	0.100
22/1800	25.5	100.2	900.9	14.6	0.060
22/2000	25.5	100.5	811.8	13.1	0.140
22/2200	25.5	100.9	793.0	14.5	0.107
23/0000	25.5	101.2	787.9	14.1	0.173
23/0200	25.8	101.4	797.9	16.0	0.302
23/0400	26.2	101.4	789.6	15.0	0.292
23/0600	26.5	101.4	806.8	16.4	0.489
23/0800	26.86	101.2	819.6	17.6	0.441
23/1000	27.2	100.9	839.6	18.9	0.385
23/1200	27.6	100.7	840.3	18.5	0.461
23/1400	27.9	100.2	821.0	16.5	0.357
23/1600	28.0	99.66	800.9	14.3	0.353

mechanism developed to move the hot, dry air off the Mexican plateau and over the Gulf of Mexico. There was one very important difference between the cases – the air over the Gulf was much cooler than the event case (generally 4 to 6 C cooler).

The event case *PV* was generated in the upper levels, over Mexico, transported down to the lower levels, then advected over central NC arriving 72 hours later at the time of a tornadic outbreak. Initially, there were two jet streaks embedded within the STJ. The first streak (located over TX and the Gulf Coast States) facilitated *PV* production and transported the *PV* southward. The second streak and its associated thermally indirect circulation transported the *PV* down to the mid levels (~ 500 hPa) over the Mexican plateau. At the same time, heating over the Mexican plateau producing a deep and warm dry adiabatic layer over MX, which was forced by large sensible heat fluxes resulting from clear skies, minimal soil moisture and arid conditions. A MPS developed over the Mexican plateau, which created ascent to 550 hPa. An area of vertical convergence was created in the 500–600 hPa layer increasing the thermal gradient (static stability) and generating *PV*. The increase in static stability was primarily responsible for the increase in mid-level *PV*. This midlevel *PV* maximum then moved eastward and a hydrostatic mountain wave transported the *PV* downward near the Mexican coast. As the *PV* maximum moved downward, it increased due to increasing static stability, tilting of horizontal vorticity into the vertical and frictional effects. The low-level *PV* moved along the Gulf Coast and finally north along the East Coast to central NC at the time of the tornado outbreak. The low-level *PV* maximum was maintained and increased by a combination of low-level wind shear, latent heating, frictional effects and sensible heating.

In the non-event, the STJ was absent, thus *PV* was not transported downward to the midlevels. The low-level wind field over the western Gulf of Mexico was from the east advecting clouds over the Mexican plateau minimizing surface heating and inhibiting a deep dry adiabatic layer. The easterly low-level flow prevented the development of mountain waves southwest of BRO inhibiting the downward transport of mid-level *PV*. In addition, the non-event case did not have a LLJ over the western Gulf of Mexico to transport northward any low-level *PV*.

There were two distinct differences between the cases. First, the *PV* maximum was a coherent and traceable entity over 72 hours in the event case while in the non-event case the *PV* maximum was not a coherent, long-lasting entity. Second, the event case *PV* maximum originated ~ 1500 km to the south than that of the non-event case.

Acknowledgements

The first author would like to thank the Air Force Institute of Technology for the opportunity to pursue my advanced degree. The authors wish to thank Drs Robert Rozumalski and Kenneth Waight III of MESO Inc. for access to and help with the MASS model.

References

Daley R (1991) Atmospheric Data Analysis. Cambridge: Cambridge University Press, 457 pp

Danielsen E (1968) Stratospheric-tropospheric exchange based on radioactivity, ozone, and potential vorticity. J Atmos Sci 25: 502–518

Gidel LT, Shapiro MA (1979) The role of clear air turbulence in the production of potential vorticity in the vicinity of upper tropospheric jet stream-frontal systems. J Atmos Sci 36: 2125–2138

Gonski RF, Woods BP, Korotky WD (1989) The Raleigh tornado – 28 November 1988: An operational perspective. Preprints, 12th Conf. on Weather Analysis and Forecasting, Monterey, CA Amer Meteor Soc pp 173–178

Gyakum JR, Kuo Y-H, Guo Z, Guo Y-R (1995) A case of rapid continental mesoscale cyclogenesis. Part II: Model and observational diagnosis. Mon Wea Rev 123: 998–1024

Kalnay E, Kanamistu M, Kistler R, Collins W, Deaven D, Gandin L, Iredell M, Saha S, White G, Wollen J, Zhu Y, Chelliah M, Ebisuzaki W, Higgins W, Janowiak J, Mo KC, Ropelewski C, Wang J, Leetmaa A, Reynolds R, Janne R, Joseph D (1996) The NMC/NCAR 40-year reanalysis project. Bull Amer Meteor Soc 77(3): 437–471

Kaplan ML, Paine DA (1977) The observed divergence of the horizontal velocity field and pressure gradient force at the mesoscale. It's implications for the parameterization of three-dimensional momentum transport in synoptic-scale numerical models. Beitr Phy Atmos 50: 321–330

Kaplan ML, Karyampudi VM (1992a) Meso-beta numerical simulation of terrain drag-induced along-stream circulations. Part I: Midtropospheric frontogenesis. Meteor Atmos Phys 49: 133–156

Kaplan ML, Karyampudi VM (1992b) Meso-beta numerical simulation of terrain drag-induced along-stream circulations. Part II: Concentration of potential vorticity within dryline bulges. Meteor Atmos Phys 49: 157–185

Kaplan ML, Zack JW, Wong VC, Tuccillo JJ (1982a) Initial results from a mesoscale atmospheric simulation system and comparisons with the AVE-SESAME I data set. Mon Wea Rev 110: 1564–1590

Kaplan ML, Lin Y-L, Hamilton DW, Rozumalski RA (1998) The numerical simulatioin of an unbalanced jetlet and its role in the Palm Sunday 1994 tornado outbreak in Alabama and Georgia. Mon Wea Rev 126: 2133–2165

Keyser D, Shapiro MA (1986) A review of the structure and dynamics of upper-level frontal zones. Mon Wea Rev 114: 452–499

Kocin PJ, Uccellini LW, Zack JW, Kaplan ML (1985) A mesoscale numerical forecast of an intense convective snowburst along the East Coast. Bull Amer Meteor Soc 66: 1412–1424

Lin Y-L, Farley RD, Orville HD (1983) Bulk parameterization of the snow field in a cloud model. J Clm Appl Meteorol 22: 1065–1092

Lin Y-L, Wang T-A (1996) Flow regimes and transient dynamics of two-dimensional stratified flow over an isolated mountain ridge. J Atmos Sci 53: 139–158

Mahrt L, Pan H (1984) A two-layer model of soil hydrology. Bound-Layer Meteor 29: 1–20

MESO (1995) MASS Versiion 5.8 Referece Manual, MESCO, Troy, NY, 119 pp

Miles JW (1961) On the stability of heterogeneous shear flows. J Fluid Mech 10: 496–508

Murry R, Daniels SM (1953) Transverse flow at entrance and exit to jet streams. Quart J Roy Meteor Soc 79: 236–241

Newton CW (1958) Variations in frontal structure of upper level troughs. Geophysica 6: 357–375

Noaa (1988) Storm data, 30, 11: 72 pp

Noilhan J, Planton S (1989) A simple parameterization of land surface processes for meteorological models. Mon Wea Rev 117: 536–549

Reed RJ (1955) A study of a characteristic type of upper-level frontogenesis. J Meteor 12: 226–237

Reiter ER (1967) Jet Streams, Doubleday & Company, 189 pp

Rozumalski RA (1997) The role of jet streak regeneration forced by a deepening continental planetary boundary layer in the explosive surface cyclogenesis of 28 March 1984. Ph. D. Thesis, North Carolina State University, 360 pp. (Available from the corresponding author)

Tripoli GJ, Cotton WR (1989) Numerical Study of an Observed Orogenic Mesoscale Convective System. Part 1: Simulated Genesis and Comparison with Observations. Mon Wea Rev 117: 273–304

Tripoli GJ, Cotton WR (1989) Numerical Study of an Observed Orogenic Mesoscale Convective System. Part 2: Analysis of Governing Dynamics. Mon Wea Rev 117: 305–328

Uccellini LW, Johnson D (1979) The coupling of upper and lower tropospheric jet streaks and implication for the development of severe convective storms. Mon Wea Rev 107: 682–703

Uccellini LW, Koch SE (1987) The synoptic setting and possible energy sources for mesoscale wave disturbances. Mon Wea Rev 115: 721–729

Uccellini LW, Kocin PJ (1987) The interaction of jet streak circulations during heavy snow events along the East Coast of the United States. Wea & Forecasting 1: 289–308

Van Tuyl AH, Young JA, Numerical Simulation of Nonlinear Jet streak Adjustment, Mon Wea Rev, 110: 2038–2054

Whitaker JS, Uccellini LW, Brill KF (1988) A model-based diagnostic study of the rapid development phase of the Presidents' Day cyclone. Mon Wea Rev 116: 2337–2365

Zack JW, Kaplan ML (1987) Numerical simulations of the subsynoptic features associated with the AVE-SESAME I case. Part I: The preconvective environment. Mon Wea Rev 115: 2367–2393

Zang DL, Anthes RA (1982) A high resolution model of the planetary boundary layer-sensitivity tests and comparisons with SESAME-79 data. J Appl Meteor 21: 1594–1609

Zehnder JA, Keyser D (1991) The influence or interior gradients of potential vorticity on rapid cyclogenesis. Tellus 43A: 198–212

Corresponding authors' address: Dr. Yuh-Lang Lin, Department of Marine, Earth and Atmospheric Sciences, North Carolina State University, Raleigh, NC 27695-8208 (E-Mail: yl_lin@ncsu.edu)